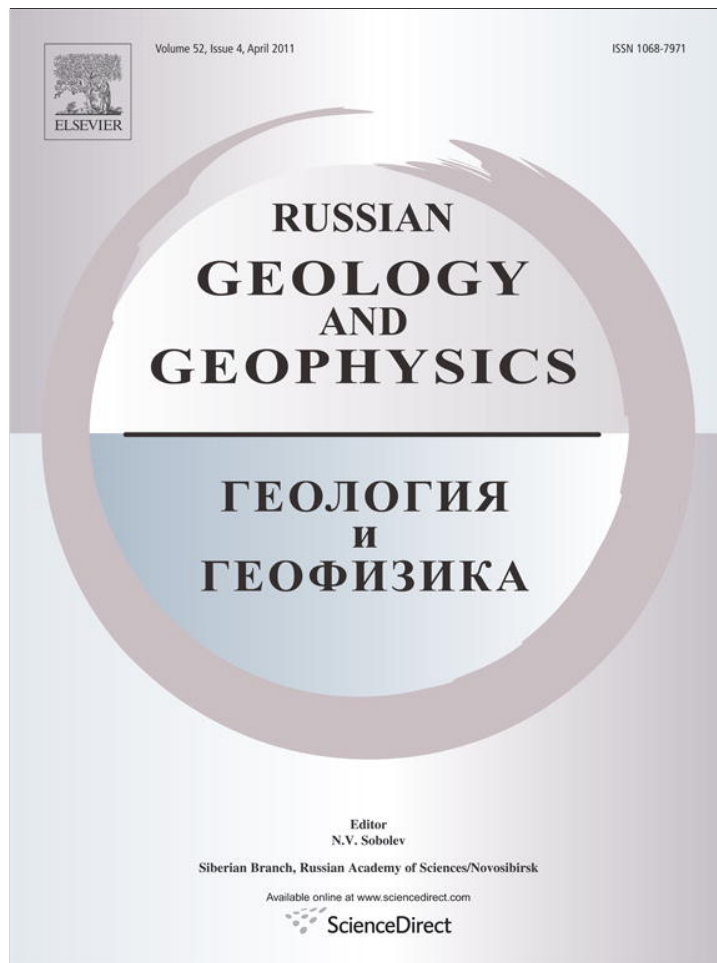


Provided for non-commercial research and education use.
Not for reproduction, distribution or commercial use.



This article appeared in a journal published by Elsevier. The attached copy is furnished to the author for internal non-commercial research and education use, including for instruction at the authors institution and sharing with colleagues.

Other uses, including reproduction and distribution, or selling or licensing copies, or posting to personal, institutional or third party websites are prohibited.

In most cases authors are permitted to post their version of the article (e.g. in Word or Tex form) to their personal website or institutional repository. Authors requiring further information regarding Elsevier's archiving and manuscript policies are encouraged to visit:

<http://www.elsevier.com/copyright>



Geochemistry, petrogenesis and geodynamic origin of basalts from the Katun' accretionary complex of Gorny Altai (southwestern Siberia)

I.Yu. Safonova^{a,b,*}, M.M. Buslov^a, V.A. Simonov^a, A.E. Izokh^a, T. Komiya^c,
E.V. Kurganskaya^a, T. Ohno^c

^a V.S. Sobolev Institute of Geology and Mineralogy, Siberian Branch of the Russian Academy of Sciences,
pr. Akademika Koptyuga 3, Novosibirsk, 630090, Russia

^b Korean Institute of Geoscience and Mineral Resources (KIGAM), 92 Gwahang-no, Daejeon, 305-350, Korea

^c University of Tokyo, 3-8-1 Komaba, Meguro-ku, Tokyo 153-8902, Japan

Received 6 August 2010; accepted 31 August 2010

Abstract

The paper presents new data on geochemistry (major and trace elements, isotopes) and petrology (composition of phenocrysts and mineral thermometry) of basalts from the Early Cambrian Katun' accretionary complex of the Kuznetsk–Altai island arc (Gorny Altai). We also discuss the geodynamic settings of the formation of basalts based on petrologic, geochemical and isotope data taking into account their relationships with associated sedimentary rocks of oceanic origin and with terrigenous sedimentary rocks of the accretionary complex. The Late Neoproterozoic basalts associated with siliceous sediments are characterized by medium TiO₂ and Zr/Nb, flat REE patterns and Nb/La_{pm} < 1 (MORB-type oceanic floor basalts). The oceanic floor basalts are represented by high- and low-magnesium varieties. The Early Cambrian basalts (Manzherok Formation) were formed in an oceanic island setting (OIB-type). They occur in sections consisting of paleo-oceanic island basalts alternated with siliceous-terrigenous-carbonate sediments of slope facies. The Manzherok basalts are characterized by high crystallization temperatures (1175 °C), and enriched incompatible elements (LREE, Ti, Nb), whose variations suggest a mantle plume source and variable degrees of partial melting in the spinel and garnet stability fields. The low to high-Mg Middle Cambrian basalts of the Ust'-Sema Formation occur as subparallel dikes and lava flows, which cut and overlap the accretionary complex. The basalts are characterized by low TiO₂, Nb, LREE, high Zr/Nb and, compared to the OIB-type basalts, lower temperatures of crystallization, 1047 °C and 1138 °C for the low- and high-Mg varieties, respectively. Geochemically, the low-Mg basalts of the Ust'-Sema Formation are close to MORB, and the high-Mg basalts—to island-arc tholeiites. Such a combination of geochemical and geological data suggest that the low-Mg basalts of the Ust'-Sema Formation formed during ridge subduction, and the high-Mg basalts formed in a suprasubduction setting, at the crust-mantle boundary. © 2011, V.S. Sobolev IGM, Siberian Branch of the RAS. Published by Elsevier B.V. All rights reserved.

Keywords: Paleo-Asian Ocean; Late Neoproterozoic–Middle Cambrian; oceanic plate stratigraphy; volcanism; subduction; accretion; basalts; mantle sources

Introduction

The origin of volcanogenic-sedimentary units from the Early Paleozoic fold belts of the western Altai–Sayan area, which includes the Katun' zone of Gorny Altai (Fig. 1), has been a topic of numerous debates for many years (e.g., Berzin et al., 1994; Buslov, 1992; Dobretsov et al., 2004; Gibsher et al., 1997; Gusev, 1991; Zybin, 2006). Buslov and his colleagues studied volcanic and sedimentary rocks with various

ages and compositions, which were tectonically juxtaposed into a single folded structure (Buslov et al., 2001). Taking into account the transpressional structure of the region, they regarded the Katun' zone as a part of the Kuznetsk–Altai island arc, which formed at a margin of the Siberian continent as a result of the Late Neoproterozoic–Cambrian subduction of the Paleo-Asian Ocean. Fragments of Early Cambrian oceanic islands and underlying Late Neoproterozoic–Early Cambrian ophiolites (Fig. 1) were incorporated into the Katun' accretionary complexes during the subduction (Buslov et al., 1993; Dobretsov et al., 2004). Later, in the Middle Cambrian, the structure of the accretionary complex were cut by dikes and their co-magmatic volcanic rocks, which, together with

* Corresponding author.

E-mail address: inna03-64@mail.ru (I.Yu. Safonova)

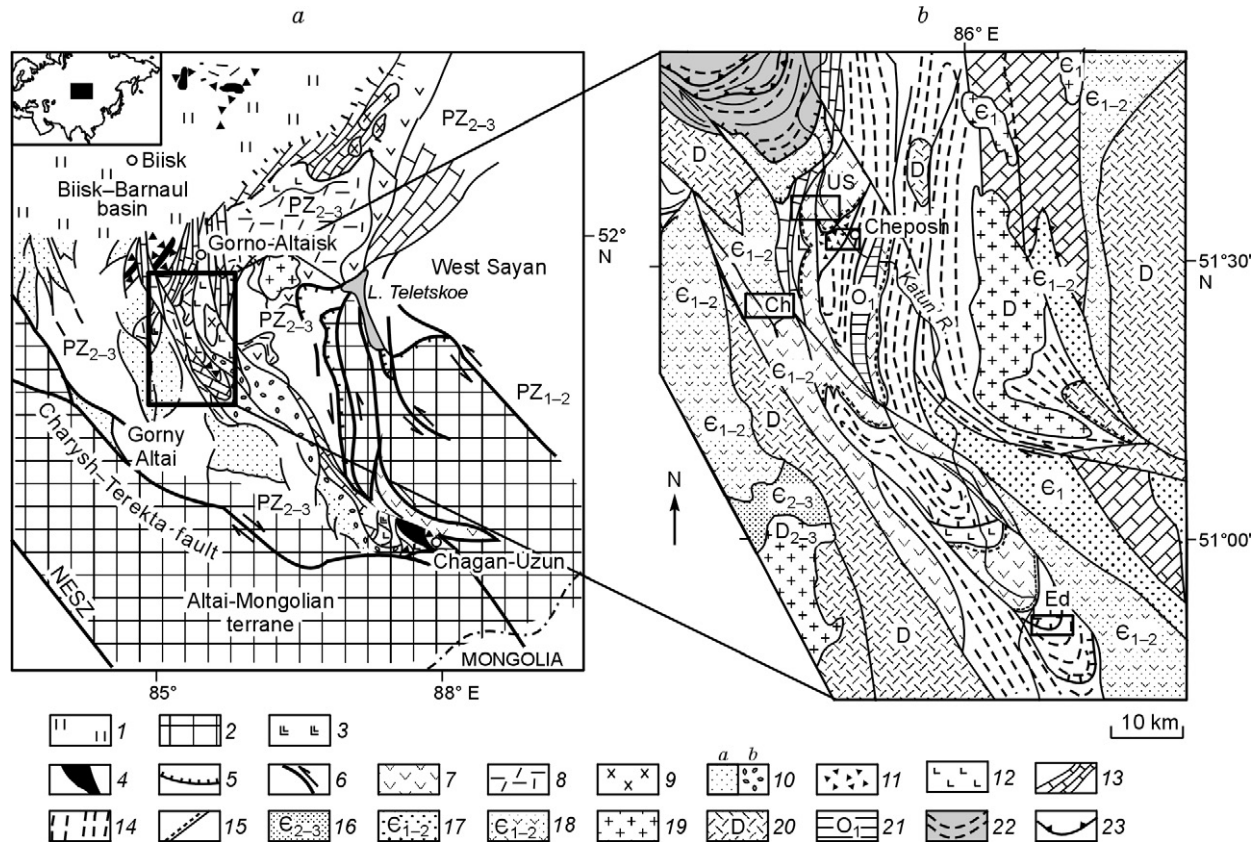


Fig. 1. *a*, Late Neoproterozoic–Cambrian island-arc and oceanic complexes of Gorny Altai in the western Altai–Sayan area (modified from Buslov et al., 2001); *b*, geological scheme of the Katun' AC (modified from Dobretsov et al., 2004). 1, Neogene–Quaternary sedimentary rocks; 2, Altai–Mongolian terrane of Precambrian age; 3, MORB-type basalts; 4, Chagan–Uzun ultramafic–gabbro massif; 5, thrust; 6, strike-slip fault; 7–10, Kuznetsk–Altai island arc of the Late Neoproterozoic–Early Cambrian age; 7, 8, volcanic rocks of tholeiite–boninite (7) and calc-alkaline (8) series; 9, gabbroids; 10, Anui–Chuya forearc basin of the Middle–Late Cambrian age (*a*, flysch; *b*, olistostrome); 11, olistostrome and melange; 12–14, paleoseamount units of Late Neoproterozoic–Early Cambrian age: 12, basalts; 13, “carbonate cap” dolomite and limestone; 14, slope facies; 15, Middle Cambrian basal conglomerate; 16–18, forearc turbidite units (16) with andesibasaltic tuffs (17) and basaltic lavas and tuffs (18); 19, granitoids; 20, volcanogenic–sedimentary rocks; 21, Ordovician sedimentary rocks; 22, Kaim Formation (allochthonous terrane); 23, Early Cambrian faults. Sampling localities: Ch, Cherga; US, Ust’-Sema; Ed, Edigan. NESZ, North-East shear zone.

associated carbonate and terrigenous rocks of the Ust’-Sema Formation, overlapped the accretionary complex. From a geodynamic point of view, the Late Neoproterozoic–Early Cambrian tholeiitic, subalkaline and alkaline basalts were interpreted as tectonically disintegrated fragments of the oceanic crust of the Paleo-Asian Ocean (Buslov et al., 1993; Dobretsov et al., 1995, 2004; Safonova et al., 2004, 2009), whereas the origin of younger basalts was attributed either to the magmatism of island arcs (Buslov et al., 1993) or back-arc basins (Gibsher et al., 1997) or continental margin rifting (Zybin, 2006).

The geochemical characteristics of basalts are of special interest for understanding geodynamic settings of their formation, compositions of their mantle sources and petrogenesis (e.g., Kerrich and Wyman, 1997). Tholeiitic to alkaline intraplate basalts of oceanic islands (OIB type) form due to the activity of mantle plumes rising from the core–mantle boundary (Hofmann, 1997; Maruyama et al., 2007). They are characterized by enrichment in incompatible elements such as light rare earth elements (LREE), Ti, Nb and Th, and possess characteristic isotope compositions (Hemond et al., 1993; Hofmann, 1997; Weaver, 1991; Zindler and Hart, 1986).

OIB-type basalts have been found in Precambrian greenstone belts (e.g., Hofmann, 1997; Komiya et al., 2002, 2004; Polat et al., 1998; Thurson, 2002), and in Phanerozoic fold belts (e.g., Buslov et al., 2001, 2003; Gordienko et al., 2007; Dobretsov et al., 2004; Safonova et al., 2004, 2008, 2009). In association with mid-oceanic ridge basalts (MORB), they compose Oceanic Plate Stratigraphy (OPS) (Isozaki et al., 1990). OPS is characterized by a regular change of lithologic facies from the pelagic through hemipelagic to terrigenous environment. In the case of oceanic rises, the facies change from shallow-water limestones atop an oceanic island, through volcanoclastics and carbonate debris materials of slope facies, to siliceous mudstones and shales formed at the foothill and deep-water chert and basalts in the base of the island. The OPS units are incorporated into accretionary complexes during the subduction of the oceanic plate.

MORB-type basalts form during the decompressional melting of upper mantle material at mid-oceanic ridge and have more a homogenous composition compared to OIB-type basalts. They are characterized by medium to low Ti, LREE, Nb and Th, and have high ¹⁴³Nd/¹⁴⁴Nd and low ⁸⁷Sr/⁸⁶Sr ratios (e.g., Hart et al., 1992; Saunders et al., 1988; Zindler

and Hart, 1986). During subduction, parts of large oceanic rises may be incorporated into the accretionary complexes, whereas most of the MORB is submerged into the upper mantle. They are dehydrated to contribute to a formation of arc basalt and andesite at the subduction zone, or partly melted to form suprasubduction and/or island-arc volcanic series, especially during ridge subduction (e.g., Defant and Drummond, 1990; Weaver and Johnson, 1987).

It is more difficult to identify the origin of Precambrian and Early Paleozoic mafic volcanic rocks than their young analogues. This, first of all it is because of a probable change of the primary concentrations of mobile elements, such as Rb, Sr, Ba, Pb, K, and isotope ratios of Sr and Pb as a result of underwater basalt eruption over the oceanic floor and postmagmatic alteration (e.g., Bednarz and Schmincke, 1989; Gelinat et al., 1982; Sun and McDonough, 1989; Thompson, 1991). As a result, more reliable information about oceanic magmatism can be obtained by the study of concentrations of relatively immobile incompatible elements, in particular the LREE-Nb-Th (e.g., Floyd and Winchester, 1975; Polat et al., 1999; Saundres, 1988) and compositions of phenocrysts and their hosted melt inclusions by methods of thermobarogeochemistry, microprobe and ion-mass spectrometry (e.g., Safonova et al., 2008; Simonov et al., 2005; Sobolev, 1996, 2009).

This work presents new data on the major and trace elements and isotopic composition of basalts from the Katun' accretionary complex (AC) of Gorny (or Russian) Altai. They are Late Neoproterozoic–Early Cambrian basalts of the Paleo-Asian Ocean, which are thought to belong to the Ust'-Cherga, Eskonga and Manzherok Formations, and the Middle Cambrian basalts of the Ust'-Sema Formation. The paper also presents the first data on the composition of clinopyroxene phenocrysts in the Manzherok and Ust'-Sema basalts. The detailed geochemical characterization of the basalts allows us to conclude about their petrogenesis and mantle sources and to improve our understanding of the geodynamic nature of the three groups of volcanic rocks.

Geological outline of the Katun' accretionary complex

The Katun' zone of Gorny Altai is an accretionary complex of the Kuznetsk–Altai island arc (Fig. 1, *a*), which was formed at a margin of the Siberian continent. The formation of the Katun' accretionary complex (wedge) was related to the Late Neoproterozoic–Cambrian stage of oceanic subduction and the accretion of paleo-islands to the Kuznetsk–Altai island arc (Buslov et al., 1993, 2001; Dobretsov et al., 2004).

The Katun' accretionary complex (Katun' AC) is located in the northern Gorny (Russian) Altai and is extended to a distance of more than 120 km with a width of 30–40 km. The Katun' AC consists of tectonic sheets of volcanogenic-sedimentary units, which are interpreted as various lithological facies of the Early Cambrian Katun' paleoseamount and underlying Late Neoproterozoic–Early Cambrian rocks of oceanic floor and ophiolites (Fig. 1, *b*) (Dobretsov et al., 2004; Safonova et al., 2004, 2009). The fragments of ophiolites are

basalt-siliceous units of a mid-oceanic ridge (MOR), which have been identified as elements of the Early Cambrian Ulus-Cherga and, possibly, Early Cambrian Eskonga and Manzherok Formations. The MORB units occur in the lower parts of the sections of the volcanogenic-sedimentary units. In general, the basalt-sedimentary units represent three groups of rocks, which formerly belonged to paleo-oceanic island units in oceanic plate stratigraphy: (1) basalt-siliceous-clay rocks of the main body of the island including its base, (2) slope facies carbonate-siliceous-terrigenous-basalt breccia, and (3) massive and micritic limestones of island top (carbonate cap). Besides, the Katun' AC includes the Middle Cambrian basalts and sedimentary rocks of the Ust'-Sema Formation. The basalts occur as dikes and lava flows, which, together with sedimentary rocks, form a volcanic structure superimposed on the rocks of the accretionary complex.

The Early Cambrian age of the paleo-oceanic island is reliably constrained from the occurrences of microphytolites, algae and siliceous sponge spicules in the slope facies sediments (Postnikov and Terleev, 2004). The units of the Katun' AC are unconformably overlain by basaltic conglomerates of the Shashkular Formation, which consists of predominantly carbonate rocks and subordinate amounts of basaltic conglomerate. The Shashkular carbonate rocks in the Shashkular and the overlying reefal limestones of the Cheposh Formation contain Early Cambrian archaeocyaths and trilobites. The boulders and pebbles of the basaltic conglomerate consist of the rocks transported from the accretionary prism: basalt, dolomite, limestone and siliceous shale. Stratigraphically higher occurs the Middle Cambrian Ust'-Sema Formation, which consists of lavas, tuffite, tuffaceous sandstone and siliceous-carbonate rocks. The Ust'-Sema Formation is overlain by the Elandin Formation, containing Middle Cambrian trilobites (Repina and Romanenko, 1978; Zybin, 2006). The dikes of olivine-pyroxene and pyroxene-plagioclase porphyritic basalts, dolerites and gabbro are comagmatic to the lavas of the Ust'-Sema Formation and cut the rocks of the accretionary wedge, Shashkular, and Cheposh Formations. The dikes often occur parallel to each other and the thickness of individual dikes reaches several meters and that of dike clusters up to 5–10 meters. The NS-striking dikes have been found over the whole territory of the Katun' zone, at a distance of more than 100 km from Ust'-Sema Village in the north to the Edigan River in the south (Fig. 1, *a*) (Buslov et al., 1993; Gibsher et al., 1997; Zybin, 2006).

Detailed geochemical and petrologic studies have been performed for three groups of basalts: (1) Early Cambrian oceanic island basalts of the Manzherok Formation; (2) Late Neoproterozoic–Early Cambrian oceanic floor basalts in separate sections of the Ulus-Cherga, Eskonga, and Kaim Formations; (3) Middle Cambrian basaltic lavas and dikes of the Ust'-Sema Formation. The composition and geodynamic settings of the formation of these three groups of basalts were briefly discussed before (Buslov et al., 2001; Dobretsov et al., 2004; Gibsher et al., 1997; Safonova, 2009; Safonova et al., 2004, 2009). In the present paper, identification of geodynamic settings of the formation of basalts are based on their clarified

geological position and detailed analysis of geochemical (major, trace and rare-earth elements), isotopic and petrologic data.

Analytical methods

The analyses of clinopyroxenes and their melt inclusions were made with a Cameca CAMEBAX electron microprobe running at a beam current of 40 mA and acceleration voltage of 20 kV. The beam width was usually about 2 μm and was defocused for glass blue diopside analyses.

Samples for geochemical analyses were obtained from the least altered and deformed outcrops of pillow-lavas and flows. Most analyses were made at the Institute of Geology and Mineralogy, Siberian Branch, Russian Academy of Science. Abundances of major and trace elements (Rb, Sr, Ba, V, Ni, Zn, Ga, Y, Zr, and Nb) were determined by X-ray fluorescence (XRF) using a "Nauchpribor" spectrometer (analytical procedure following the Russian state analytical standard OST-41-08-212-82 Mingeo SSSR). Abundances of high-field strength elements (HFSE), rare-earth elements (REE), large-ion lithophile elements (LILE) and major elements (Na, Ca, Fe) in samples E4068–U4133 and T4006–T4044 were determined by instrumental neutron activation analysis (INAA) using Ge detectors for γ -rays higher than 30 keV and below 2000 keV. The samples were radiated using a nuclear reactor of the Tomsk Polytechnical University by an integral flux of 10^{17} neutrons/cm². The measurements were made on a gamma-spectrometer in two cooling stages of 1 week and 3 months. The concentrations of Y, Zr, Nb, Ti, Rb, Sr, Pb, V, Mn, Ni, Cu, Zn were also determined by SR XRF (synchrotron radiation XRF) (Bobrov et al., 1998; Phedorin et al., 2000).

Trace elements (REE, HFSE and LILE) in samples Kat-34-07–Kat-61-07 were analyzed by inductively coupled plasma mass-spectrometry (ICP-MS) in the Tokyo Institute of Technology (ThermoElemental VG 244 PlasmaQuad 2 LA ICP MS; on fused glass beads) and in the Institute of Geology and Mineralogy SB RAS (Finnigan Element ICP MS device; on powdered samples) using the protocols of (Jenner et al., 1990). The glass beads were made by fusing a mixture consisting of 1 part of basalt powder and 10 parts of lithium tetraborate on a Rigaku furnace. The powdered samples were dissolved using a HF-HNO₃ (2:1) mixture in a screw-top Teflon beaker for 2 days at ~100 °C followed by evaporation to dryness, refluxing in 6N HCl and drying twice, and then dissolution in 1N HCl. The procedure was repeated until the powder was completely dissolved. The final solution was evaporated to dryness, refluxing in 6N HNO₃ and drying three times, and dissolved in 2% HNO₃. Wet chemical procedures were conducted under clean lab conditions. BHVO-1, BCR-1 and JB-3 were used as international reference materials to estimate precision and accuracy. The analytical errors are estimated as 2–7% for REE and HFSE.

The isotopic compositions of Sm, Nd, Sr, and Rb in samples 242/2 and 92-C-1 were analyzed at the Vernadsky Institute of Geochemistry and Analytical Chemistry RAS

(GEOHI) using a TRITON mass spectrometer (Laboratory of Radiogenic Isotopes) and in the Tokyo Institute of Technology (Titech) using a multicollector mass-spectrometer (MC ICP MS) equipped with Nu Plasma 500 device (samples Kat-34-07, Kat-52-07, Kat-55-07). In the GEOHI the concentrations of Rb, Sr, Sm, and Nb were determined by the isotope dilution method. The samples were decomposed in an HF + HNO₃ mixture at a temperature of 200 °C for two days using titanium autoclaves with Teflon inserts. The sample was spiked before decomposition with a mixed ⁸⁵Rb + ⁸⁴Sr tracer. The separation of Rb, Sr, and all rare-earth elements was carried out by ion exchange chromatography using Teflon columns with 3.5 ml of Dowex 508 resin and 2.3N HCl as an eluent. Nd and Sm were separated on Eichrom Ln-spec columns by stepwise elution with 0.5N and 0.75N HCl, respectively. The long-term precision of isotopic analysis was controlled using international standards: SRM-87 for Sr and La Jolla for Nd. The obtained isotopic ratios are ⁸⁷Sr/⁸⁶Sr = 0.710256 ± 18 (*N* = 21) and ¹⁴³Nd/¹⁴⁴Nd = 0.511843 ± 11 (*N* = 19).

In the Tokyo Institute of Technology Sr and Nd isotopes were measured using a special device Aridus (Cetac, Omaha, USA) to improve desolvating. The samples were dissolved during 24 hours in a mixture of acids (HF and HClO₄) according to the procedure described in (Yokoyama et al., 1999). Sr and REE were separated from the matrix using Sr-spec and TRU-spec resins, respectively, and then Nd was separated with Ln-spec resin (Pin and Zalduogui, 1997; Pin et al., 1994). The chemical separation was performed according to a standard technique of ion exchange. The Sr and Nd isotope ratios were corrected by normalizing to ⁸⁶Sr/⁸⁸Sr = 0.1194 and ¹⁴⁶Nd/¹⁴⁴Nd = 0.7219 and using standards SRM 987 and JNdi-1 for Sr and Nd, respectively.

Sample description

The samples of Groups 1 and 2 were selected in the Katun' River basin, at the Edigan (nos. Kat-45-07, Kat-49-07, Kat-50-07, Kat-51-07, Kat-52-07, Kat-53-07, Alt-112-08, E4091-E40111, 9-160; the Cheba–Edigan watershed), Cheposh (Kat-54-07, Kat-55-07) and Cherga (242/2, Kat-34-07, Kat-38-07, Kat-40-07) sites. The samples of the third group were selected near Ust'-Sema Village (T4006-T4044, Kat-56-07, Kat-58-07, Kat-60-07, Kat-61-07) (Fig. 1, *b*). Samples E4091–E40111 and 9-160 were taken along the Cheba River at the base of the Manzherok Formation and, possibly, they are oceanic floor basalts overlapped by oceanic island volcanogenic-sedimentary units. Sample G204 can also be referred to oceanic floor basalts because it was taken west of Gorno-Altai (Fig. 1), within a part of the accretionary complex, which was earlier shown to contain oceanic crust fragments (Zybin, 2006).

Petrography and mineralogy

The typical features of the Late Neoproterozoic–Early Cambrian basalts of Groups 1 and 2 are dark green and dark

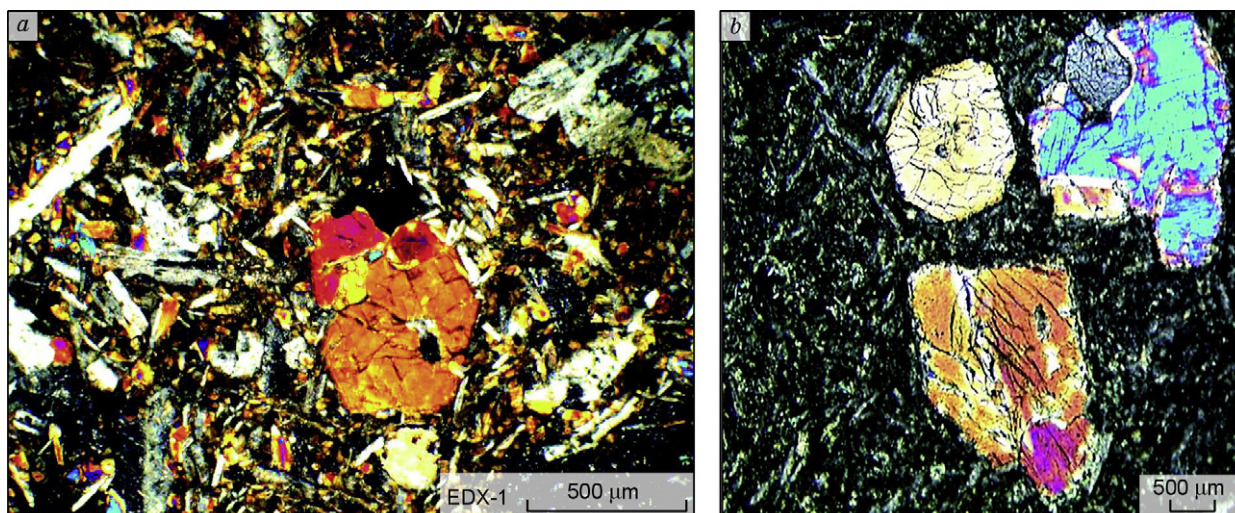


Fig. 2. Photos of thin sections of Manzhherok (a) and Ust'-Sema (b) basalts, showing pyroxene phenocrysts (nicols crossed).

gray color, massive or, less often, amygdaloidal structure. The most abundant petrographic varieties are dolerite and diabase porphyrite, aphyric and fine-porphyritic basalts with rare phenocrysts of clinopyroxene and plagioclase up to 1 mm size (Fig. 2, a). The volcanic rocks underwent strong secondary alteration, which resulted in chloritization, amphibolitization and albitization of rocks. The Middle Cambrian Ust'-Sema basalts (third group) are large-porphyritic dark gray volcanics with greenish phenocrysts of clinopyroxene up to 5 mm across (Fig. 2, b).

Relict clinopyroxene phenocrysts were analyzed in two samples of the Middle Cambrian Ust'-Sema basalts (C-72g-04 and C-73a-04) and in one sample of the Early Cambrian Manzhherok basalt (Kat-55-07). Microscopically, the pyroxene grains have a well-preserved euhedral shape (Fig. 2); most grains are angular or rectangle and contain melt microinclusions.

The clinopyroxenes are diopside ($Wo_{38-42}En_{42-52}Fs_{0-12}$) in sample C-73g-04, diopside-salite ($Wo_{34-41}En_{38-47}Fs_{1-12}$) in C-73a-04, and diopside-augite ($Wo_{31-38}En_{45-49}Fs_{6-12}$) in Kat-55-07 on a ternary diagram of wollastonite (Wo), enstatite (En) and ferrosilite (Fs) (Fig. 3, a).

Generally, the composition of the clinopyroxene of mafic lavas is controlled by the composition of initial magmatic melts, thus allowing us to reconstruct the composition of their mantle source (Nisbet and Pearce, 1977). Figs. 3, c–e show the compositions of the clinopyroxenes from Katun' basalts compared with those from modern basalts of oceanic islands (OIB) and MORB (Komiya et al., 2002) and from the Late Neoproterozoic intraplate basalts of the Kurai paleoseamount of Gorny Altai, which is located 300 km southeast of the Katun' paleoseamount (Safonova et al., 2008). The compositions of clinopyroxenes from the modern OIB and MORB are clearly different at high Mg# (Fig. 3, c–e). Although clinopyroxenes in the ancient MORB and OIB have different compositions from the modern equivalents, the pattern of

differences in their composition between them is similar to those in the modern equivalents (Komiya et al., 2002).

The clinopyroxenes of the Ust'-Sema Formation are characterized by Ti decreasing with Al increasing (Fig. 3, c) and Cr decreasing with Mg# increasing (Fig. 3e), which suggest minor fractionation of opaque oxides, e.g., titanomagnetite, whereas the simultaneous increase of Mg# and Al (Fig. 3, d) implies the growth of ferrosilite mineral during crystallization. The compositional points of pyroxenes from two samples of the Ust'-Sema Formation form two separate groups in the Wo–En–Fs and Mg#–Na diagrams (Fig. 3, a, e). The pyroxenes from sample C-72g-04 contain more Si, K, Mg, but less Ti, Cr, Fe, Na, than the pyroxenes from sample C-73a-04 (Table 1). Their hosting basalts possess similar compositional differences except for Cr and K (Table 4), suggesting fractionation of these elements from the melt during pyroxene crystallization.

The almost 30% variation of Ti at less variable Al (Fig. 3, c) and the two separate clusters of points in the Mg#–Cr plot (Fig. 3e) in the pyroxenes of the Manzhherok basalts can be related to relatively wide variations of Ti concentrations at relatively narrower variations of Al, Cr, and Mg in plume-related basaltic melts (Regelous et al., 2003; Safonova, 2008). Generally, the pyroxenes from the Ust'-Sema basalts are characterized by lower Ti and Al and higher Cr and Ca than those from the Manzhherok basalts (Fig. 3; Table 1).

The Ti/Al ratios in the Ust'-Sema pyroxenes (>0.15) are higher than those in the Manzhherok ones (0.1–0.15) and notably higher than in MORB (0.5–1.0) (Komiya et al., 2002). The clinopyroxenes from oceanic basalts of the Kurai and Katun' accretionary complexes in Gorny Altai have similar compositions to each other and also to those in modern OIB and MORB, but are characterized by much lower Na contents at a given Mg# (Fig. 3, c–e).

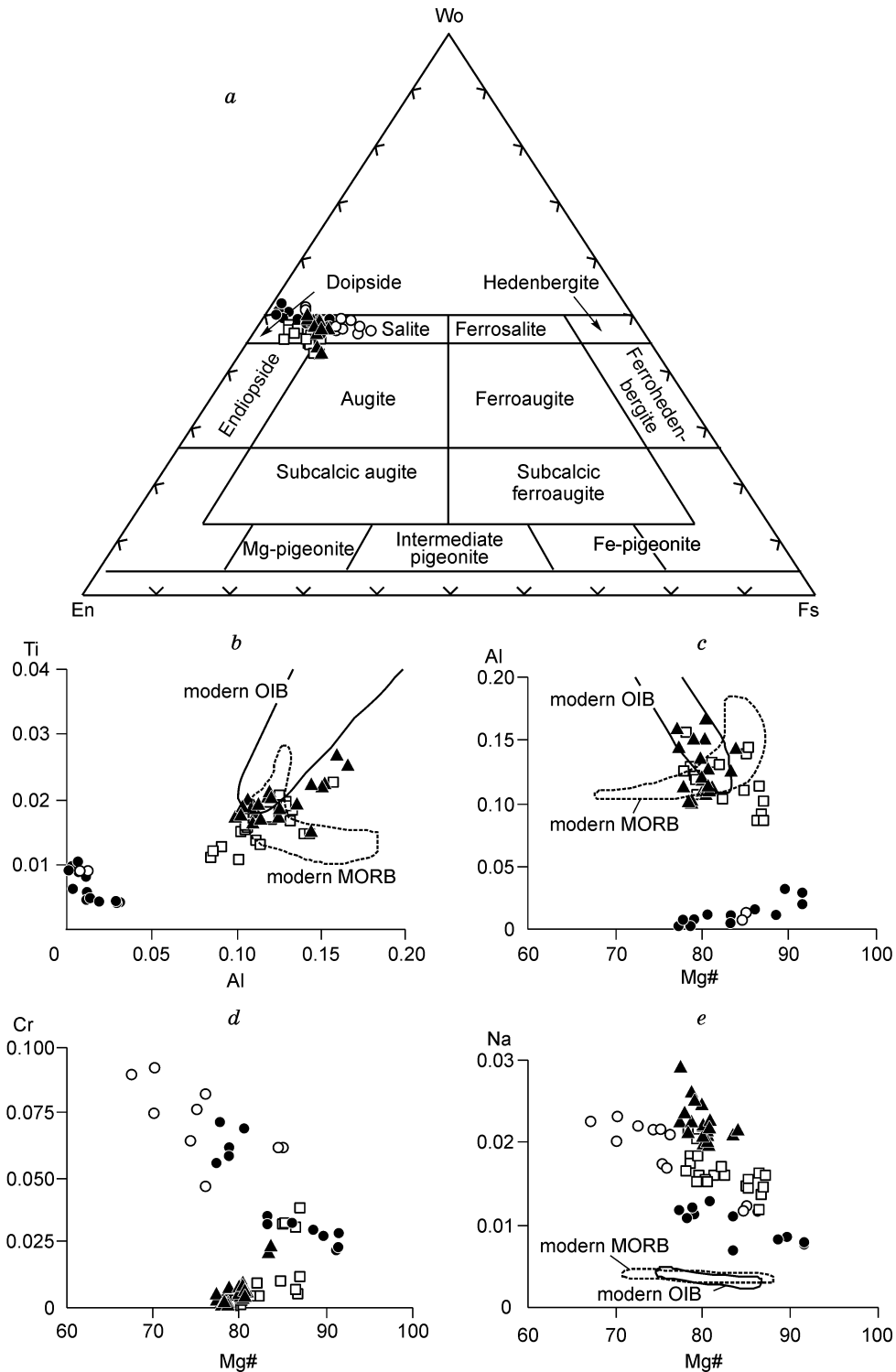


Fig. 3. Composition of clinopyroxenes from basalts of the Ust'-Sema (circles) and Manzherok (squares) Formations of the Katun' AC. a, En–Wo–Fs triangle diagram; b–e, binary plots: Al vs. Ti (b); Mg# vs. Al (c); Mg# vs. Cr (d), Mg# vs. Na (e) (atoms p.f.u. based on 6 oxygens). The boundaries of modern OIB and MORB fields are from (Komiya et al., 2002). The compositions of relict clinopyroxenes from basalts of the Kurai paleoseamount in southern Gorny Altai are given for comparison (Safonova et al., 2008).

Geochemistry of basalts

Forty representative analyses of the three groups of Katun' basalts (Tables 2–4) have been selected for geochemical characterization. According to the SiO₂ and total alkali

(Na₂O + K₂O) contents, the samples are basalt, trachybasalt and andesitic basalt. In the SiO₂ and Nb/Y diagram (Winchester and Floyd, 1977), which is more reliable because Nb and Y are less mobile during secondary alteration, the samples of Group 1 plot in the field of alkaline basalt (Manzherok

Table 1. Composition of clinopyroxene phenocrysts from basalts of the Katun' accretionary complex: mean values and ranges

Component	Manzherok Fm.		Ust'-Sema Fm.	
	Kat-55-07 (N = 20) min–max [mean]	C-72g-04 (N = 13) min–max [mean]	C-73-04 (N = 11) min–max [mean]	
SiO ₂	50.78–53.12 [51.72]	51.3–55.03 [53.07]	49.55–52.18 [50.79]	
TiO ₂	0.391–0.815 [0.57]	0.154–0.374 [0.24]	0.331–0.713 [0.51]	
Cr ₂ O ₃	0.014–1.32 [0.34]	0.761–2.44 [1.44]	1.58–3.85 [2.68]	
Al ₂ O ₃	1.97–3.59 [2.67]	0.049–0.747 [0.33]	0.001–0.297 [0.05]	
FeO	4.69–8.42 [6.59]	2.92–8.24 [5.60]	5.27–11.92 [9.08]	
MnO	0.091–0.272 [0.17]	0.084–0.235 [0.17]	0.119–0.379 [0.29]	
MgO	16.08–17.78 [16.81]	15.26–18.67 [17.01]	13.62–17.14 [15.23]	
CaO	18.31–20.82 [19.62]	20.53–23.14 [21.91]	20.29–23.23 [21.40]	
Na ₂ O	0.167–0.292 [0.22]	0.097–0.177 [0.14]	0.17–0.31 [0.26]	
K ₂ O	0.001–0.02 [0.005]	0.001–0.008 [0.0069]	0.003–0.01 [0.0014]	
Total	98.11–99.33 [98.72]	97.95–100.8 [99.91]	99.36–100.85 [100.29]	
Mg#	77.91–87.05 [82.19]	77.31–91.57 [84.54]	67.29–85.07 [75.14]	

Formation), whereas those of Groups 2 and 3 plot in the field of subalkaline basalt and andesite (Fig. 4, a). In the Al₂O₃–TiO₂+FeO–MgO triangle diagram (Jensen, 1976) the subalkaline basalts of Groups 1 and 2 plot in the field of high-Fe tholeiites, whereas the third group basalts of the Ust'-Sema Formation form two clusters in the field of tholeiitic andesite and near the border with the field of high-Fe tholeiites (Fig. 4, b).

The three groups of basaltic samples are characterized by different concentrations of TiO₂: the high-Ti Group 1 (TiO_{2av.} = 2.81 wt.%), the mid-Ti Group 2 (TiO_{2av.} = 1.05 wt.%), and the low-Ti Group 3 (TiO_{2av.} = 0.65 wt.%) (Tables 2–4). The basalts of Groups 2 and 3 are characterized by iron enrichment during fractionation (Fig. 5, a). The high TiO₂ and medium-high FeO*/MgO ratio (1.6–4.0) in the Manzherok basalts correspond to the low to medium degree of crystallizational differentiation. The lower TiO₂ (0.3–0.8 wt.%) in the Ust'-Sema basalts and the presence of two subgroups with different FeO*/MgO ratio (0.9–1.2 and 1.5–2.0) suggest a higher degree of differentiation and principally different conditions of crystallization (Fig. 5, b) (Miyashiro, 1973). Group 2 basalts are compositionally close to the Ust'-Sema samples (Group 3) but have lower Al/Ti ratios (Table 3; Fig. 10). According to the content of MgO, most of

the basalts of all three groups are medium-to-low magnesian (MgO = 3–5.8 wt.%). The higher-Mg varieties have been recognized in the 2nd (8.2–9.9 wt.% MgO) and 3rd (8.3–9.8 wt.% MgO) Groups (Tables 3, 4). Thus, we regard three groups of volcanic rocks: Group 1—Early Cambrian high-Ti oceanic island basalts (Manzherok Formation), Group 2—Late Neoproterozoic–Early Cambrian medium-Ti oceanic floor basalts (parts of the Ulus-Cherga, Eskonga and Kaim Formations), Group 3—supposedly suprasubduction Middle Cambrian low-Ti andesibasalts and basalts of the Ust'-Sema Formation. There are high- and low-Mg subgroups in Groups 2 and 3.

As far as Na, K and other large-ion lithophile elements (LILE—Rb, Sr, Ba) are highly mobile during postmagmatic alteration (Humphris and Thompson, 1978), we used low-mobile high-field strength (HFSE) and rare-earth (REE) elements only for petrogenetic and geodynamic implications.

Late Neoproterozoic–Early Cambrian oceanic basalts of the Katun' accretionary complex

The Group 1 and 2 basalts of that age are characterized by relatively wide variations of Mg# and Fe₂O₃. In Group 1 basalts (Early Cambrian OIB-type basalts of the Manzherok Formation) SiO₂ spans 43.6 to 52.3 wt.% at Mg# = 39.5–60.8; Fe₂O₃ = 9.4–15.5, TiO₂ = 2.03–4.22, P₂O₅ = 0.18–1.56, Al₂O₃ = 13.4–18.1 wt.% (Table 2). The contents of TiO₂, P₂O₅, La, Sm, Th and Nb decrease with increasing Mg#. In all MgO versus major and trace elements plots (Fig. 6), Group 1 basalts have compositions similar to those of the Emperor–Hawaii Chain of Volcanoes (EHCV). Ba/Rb ratios range from 11 to 69, and Zr/Nb ratios from 3 to 12 (6.2 in average; Table 2). The chondrite-normalized REE patterns of group 1 basalts display enrichment in LREE: La_{nav} = 97.8; La/Yb_n = 2.4–20.2 (Fig. 7, a). No Eu anomalies are observed. The degree of LREE and HREE differentiation is medium to high: La/Sm_n varies from 1.2 to 3.65, and Gd/Yb_n from 1.4 to 3.6. The primitive mantle normalized multielement spectra (Fig. 8, a) show that most samples with highly differentiated REE possess positive Nb anomalies relative to La and Th (Nb/La_{pm} = 1.2–2.9; Nb/Th_{pm} = 1.6–2.5), which is a diagnostic feature of plume-related oceanic island basalts. Several multielement spectra have Y negative anomalies, which are possibly a result of garnet fractionation, because those samples are also characterized by highly differentiated HREE (Gd/Yb_n = 2.1–3.4). The increase of Th, Nb, La, and Sm with decreasing MgO is also typical of Group 1 basalts. We can recognize two subgroups of Group 1 basalts, which have different Zr/Nb ratios, degrees of enrichment in incompatible elements (Nb and LREE), and degrees of HREE differentiation at a given content of MgO (Table 7; Figs. 6, e–h, 7, and 8). Generally, the geochemical features of Group 1 basalts are consistent with their formation from a plume-related mantle source, enriched in incompatible elements, especially in HFSE and LREE.

In Group 2 (Late Neoproterozoic–Early Cambrian MORB-type basalts) the contents of SiO₂ vary from 45.1 to 52.6 wt.%

Table 2. Concentrations of major (wt.%) and trace (ppm) elements in basalts of the Manzherok Formation of the Katun' AC (Group 1)

Sample	Kat-34-07	Kat-38-07	Kat-40-07	Kat-55-07*	Kat-45-07	Kat-49-07	Kat-50-07	Kat-51-07	Kat-52-07	Kat-53-07	Kat-54-07	92-C-1
	1	2	3	4	5	6	7	8	9	10	11	12
SiO ₂	48.90	45.78	47.37	48.47	47.78	43.79	49.23	47.10	47.43	44.96	44.56	52.32
TiO ₂	2.03	2.22	2.29	2.52	4.22	3.65	3.99	2.50	2.55	2.86	3.58	2.26
Al ₂ O ₃	13.65	14.42	13.41	14.24	16.63	13.39	14.17	16.53	15.38	18.12	15.72	12.44
Fe ₂ O ₃	12.57	14.73	13.04	12.69	12.54	14.38	11.56	14.04	14.61	11.86	14.10	11.11
MnO	0.13	0.15	0.10	0.12	0.09	0.20	0.14	0.15	0.19	0.18	0.26	0.10
MgO	7.10	6.36	6.44	6.86	3.14	4.62	4.60	3.17	3.57	6.01	8.06	6.19
CaO	9.63	11.34	10.30	8.14	4.96	8.12	7.43	6.27	5.77	7.83	5.94	7.60
Na ₂ O	0.34	0.12	0.10	0.32	1.62	2.15	2.49	1.95	2.08	1.38	2.01	5.04
K ₂ O	2.83	1.90	2.97	3.87	4.52	2.49	2.64	3.91	3.14	2.52	2.43	0.68
P ₂ O ₅	0.18	0.21	0.29	0.34	0.71	1.56	0.55	1.04	1.23	0.51	0.49	0.29
L.O.I.	2.87	3.55	4.24	2.93	3.12	4.03	2.77	1.46	3.17	3.97	2.70	2.76
Total	100.2	100.6	100.6	100.5	99.3	98.6	99.7	98.6	99.1	100.0	99.8	100.8
Mg#	50.4	43.7	47.1	49.3	31.1	36.6	41.7	28.9	30.5	47.7	50.7	52.7
La	8.9	10.8	14.2	12.8	43.8	54.4	37.0	69.8	73.5	38.5	36.0	13.0
Ce	25.6	29.0	35.9	28.2	98.7	115.4	83.4	139.0	158.2	82.7	79.1	29.0
Nd	15.6	15.7	20.2	17.2	49.3	58.3	43.2	65.4	79.1	38.4	44.0	20.0
Sm	3.9	5.7	6.4	4.7	11.9	14.5	10.9	14.7	17.4	8.2	9.9	5.4
Eu	1.46	1.89	2.29	1.71	3.75	4.72	3.31	4.74	5.24	2.88	3.58	1.4
Gd	3.9	3.3	3.7	4.1	12.5	15.7	13.4	17.2	16.1	11.7	13.7	5.7
Tb	0.60	0.95	1.20	0.72	1.66	1.88	1.48	2.04	2.68	1.22	1.34	0.8
Dy	3.5	5.7	6.6	4.7	8.3	9.4	7.9	10.1	13.8	5.8	6.8	–
Ho	0.78	0.91	1.07	0.87	1.43	1.56	1.15	1.58	2.16	0.87	0.87	–
Er	1.7	2.7	2.9	2.2	3.3	4.3	3.3	4.3	6.4	2.4	2.5	–
Tm	0.25	0.49	0.55	0.30	0.62	0.69	0.48	0.74	1.04	0.45	0.36	–
Yb	1.6	3.0	4.1	1.9	3.5	4.4	3.0	4.7	7.2	2.8	2.6	2.1
Lu	0.22	0.43	0.42	0.30	0.60	0.65	0.41	0.73	1.12	0.39	0.35	0.3
Sc	26	31	28	26	20	20	25	18	20	25	29	–
Co	44	45	40	41	32	28	36	30	21	38	60	63
Cs			0.01	0.87	0.53	0.17	0.13	0.42	1.21	1.90	2.13	–
Hf	3.8	4.4	5.6	3.9	10.9	6.7	9.7	9.0	11.5	5.0	6.4	3.8
Ta	0.63	0.87	1.02	1.01	5.34	3.82	3.42	4.95	4.46	2.35	2.25	1
Th	0.56	1.03	1.29	0.89	3.88	3.93	3.96	5.48	5.71	3.73	2.75	1
U	0.58	0.02	0.20	0.51	0.91	0.93	0.98	1.37	1.26	0.69	0.95	0.40
Ba	52	29	44	112	669	873	741	906	711	704	834	144
Rb	3.0	0.8	1.1	7.4	49.7	35.9	67.2	37.0	43.0	60.7	73.6	7
Sr	386	455	511	428	637	591	607	859	581	604	694	120
Y	18.4	28.4	35.5	21.0	42.7	48.7	37.5	52.4	74.7	30.0	31.6	29
Zr	155	167	222	157	463	251	372	419	509	215	273	154
Nb	10.3	14.2	17.9	16.7	89.0	68.6	57.7	109.1	91.3	53.1	49.6	20
Nb/Y	0.56	0.50	0.50	0.80	2.09	1.41	1.54	2.08	1.22	1.77	1.57	0.69
Ba/Rb	17	37	39	15	13	24	11	24	17	12	11	22
Zr/Nb	15	12	12	9	5	4	6	4	6	4	6	8
Al ₂ O ₃ /TiO ₂	6.7	6.5	5.9	5.7	3.9	3.7	3.6	6.6	6.0	6.3	4.4	5.5
Sr/Y	21.0	16.0	14.4	20.4	14.9	12.1	16.2	16.4	7.8	20.1	21.9	4.2
(La/Sm) _n	1.43	1.20	1.40	1.96	2.32	2.36	2.14	2.98	2.66	2.95	2.29	1
(Gd/Yb) _n	1.99	1.59	1.44	1.80	2.91	2.45	3.58	2.95	1.82	3.44	4.24	2.2
(La/Yb) _n	3.77	2.46	2.37	4.66	8.50	8.38	8.27	9.97	6.94	9.43	9.31	3.37
(Nb/La) _{pm}	1.26	1.26	1.21	1.45	1.96	1.22	1.50	1.51	1.20	1.33	1.33	1.5
(Th/La) _{pm}	0.68	0.77	0.73	0.66	0.72	0.58	0.86	0.64	0.63	0.78	0.62	0.65
(Nb/Th) _{pm}	1.84	1.64	1.65	2.19	2.73	2.08	1.74	2.37	1.91	1.69	2.15	2.27

Note. Tables 2–4 present the most complete datasets. A number of samples have been analysed only for major elements. XRF data on Nb, Y, Zr, Rb, Sr, Ba are available for several Ust'-Sema samples. We used all available geochemical data for plotting (Figs. 4–10). Variably incompatible element enriched subgroups: 1–4 (less) and 5–12 (more). * In this sample we analysed the composition of clinopyroxene phenocrysts.

Table 3. Concentrations of major (wt.%) and trace (ppm) elements in basalts of the Ulus-Cherga and Eskonga Formations (Group 2) of the Katun' AC

Sample	E4091	E4092	E4104	E4111	9-160	G204	242/2
	1	2	3	4	5	6	7
SiO ₂	45.12	46.75	46.79	48.34	52.64	51.04	47.10
TiO ₂	0.72	0.78	0.9	1.03	1.52	1.4	1.00
Al ₂ O ₃	13.78	15.15	14.85	13.27	16.78	14.6	15.60
Fe ₂ O ₃	11.23	11.89	11.26	12.11	11.89	12.07	11.40
MnO	0.21	0.24	0.24	0.18	0.14	0.251	0.17
MgO	9.93	9.46	9.3	8.22	2.93	4.92	5.02
CaO	12.33	7.02	9.8	8.79	2.20	6.65	14.19
Na ₂ O	2.04	2.53	2.56	2.58	6.35	7.07	1.85
K ₂ O	0.22	1.28	0.2	2.13	2.62	0.32	0.80
P ₂ O ₅	0.14	0.16	0.15	0.21	0.66	0.155	0.11
L.O.I.	4.12	4.40	3.42	3.32	2.86	1.9	2.82
Total	99.8	99.7	99.5	100.2	100.6	100.38	100.1
Mg#	63.9	61.4	62.3	57.6	33.0	44.9	46.8
La	4.2	3.9	4.5	5.3	3.7	5.7	7.1
Ce	10.1	9.7	11.1	12.0	9.7	15.2	17.1
Nd	6.8	6.9	7.7	7.8	7.2	9.3	11.0
Sm	2.1	2.2	2.4	2.3	2.4	3.4	3.2
Eu	0.75	0.70	0.88	0.89	1.03	1.47	1.5
Gd	2.7	2.7	3.0	2.8	3.2	4.6	4.3
Tb	0.47	0.48	0.54	0.49	0.59	0.79	0.7
Yb	1.6	1.7	2.1	1.7	0.6	2.7	2.1
Lu	0.23	0.25	0.32	0.25	0.40	0.39	0.3
Sc	80	43	45.0	38.6	46	39.47	42
Cr	219	210	307	207	115	158	295
Co	53	51	44	45	46	36	–
Cs	–	–	0.9	0.3	–	0.37	–
Hf	1.4	1.3	1.5	1.6	1.4	2.1	3.30
Ta	0.20	0.20	0.2	0.2	0.11	0.12	0.70
Th	0.5	0.6	0.6	0.5	0.4	0.63	0.6
U	0.6	0.9	0.5	0.4	0.3	0.4	–
Ba	100	740	290	740	430	–	198
Rb	0.3	9.3	1.1	25.2	12.4	–	13.0
Sr	120	364	33	274	183	–	140.0
Y	13.5	20.0	22.9	18.6	28.4	–	26.0
Zr	38	64	66	55	60	–	69.0
Nb	2.0	2.6	2.2	1.7	2.4	–	1.0
Nb/Y	0.15	0.13	0.10	0.09	0.08	–	0.04
Ba/Rb	333	80	274	29	35	–	15
Zr/Nb	19	25	30	32	25	–	69
Al ₂ O ₃ /TiO ₂	19.1	19.4	16.5	12.9	11.0	10.4	15.6
Sr/Y	8.9	18.2	1.5	14.8	6.4	–	5.4
(La/Sm) _n	1.3	1.1	1.2	1.5	1.0	1.1	1.4
(Gd/Yb) _n	1.4	1.3	1.2	1.3	1.7	1.4	1.6
(La/Yb) _n	1.8	1.6	1.4	2.1	1.6	1.4	2.3
(Nb/La) _{pm}	0.5	0.6	0.5	0.3	0.6	–	0.2
(Th/La) _{pm}	1.0	1.2	1.1	0.8	0.9	–	0.7
(Nb/Th) _{pm}	0.5	0.5	0.4	0.4	0.7	–	0.2

Note. Subgroups: high-Mg (1–4) and low-Mg (5–7).

Table 4. Concentrations of major (wt.%) and trace (ppm) elements in basalts of the Ust'-Sema Formation (Group 3) of the Katun' AC

Sample	T4006	T4014	T4017	T4044	C-72g-04*	C-73a-04*	T4035	T4042	Kat-56-07	Kat-58-07	Kat-60-07	Kat-61-07
	1	2	3	4	5	6	7	8	9	10	11	12
SiO ₂	49.88	48.12	47.48	46.82	49.93	47.55	49.9	45.03	46.57	46.45	54.19	48.43
TiO ₂	0.72	0.59	0.59	0.58	0.46	0.79	0.65	0.69	0.89	0.82	0.53	0.59
Al ₂ O ₃	14.61	13.42	15.31	14.59	11.31	14.32	19.98	20.61	21.29	18.88	15.85	20.43
Fe ₂ O ₃	9.89	12.27	10.26	10.34	11.18	12.68	9.12	11.22	11.20	10.26	8.50	9.16
MnO	0.19	0.18	0.18	0.22	0.18	0.21	0.17	0.2	0.19	0.17	0.15	0.15
MgO	8.29	9.78	8.75	8.33	9.33	6.57	5.31	5.3	4.96	5.41	4.27	4.20
CaO	8.39	8.44	9.28	9.65	12.04	10.49	7.01	9.51	6.00	10.97	8.06	8.66
Na ₂ O	2.68	2.09	3.2	2.41	1.14	2.15	2.76	2.31	1.93	0.15	0.43	0.74
K ₂ O	1.09	0.59	0.94	2.63	1.24	2.86	1.43	0.84	3.13	2.41	4.34	4.13
P ₂ O ₅	0.21	0.22	0.1	0.20	0.13	0.19	0.23	0.16	0.28	0.23	0.19	0.10
L.O.I.	3.76	4.32	4.96	4.00	2.77	3.29	3.16	4.18	4.00	4.68	4.06	3.69
Total	99.7	100.0	101.1	99.8	99.7	101.2	99.7	100.1	100.4	100.4	100.6	100.6
Mg#	62.6	61.5	63.0	61.7	60.0	48.3	53.8	48.6	44.4	48.7	47.5	45.2
La	6.6	4.1	2.9	5.6	–	–	5.7	3.9	3.9	4.0	4.9	2.8
Ce	12.0	9.1	7.0	12.0	–	–	13.1	9.1	10.2	9.2	10.0	6.7
Nd	7.9	5.8	4.9	7.6	–	–	8.4	6.1	8.0	4.6	4.0	2.8
Sm	2.4	1.6	1.5	2.1	–	–	2.4	1.8	2.9	2.1	1.7	1.1
Eu	0.8	0.5	0.6	0.8	–	–	0.9	0.9	1.3	0.8	0.7	0.4
Gd	2.9	2.0	1.9	2.5	–	–	2.9	2.2	8.3	1.8	2.4	2.4
Tb	0.5	0.4	0.4	0.4	–	–	0.5	0.4	0.8	0.4	0.3	0.2
Dy	–	–	–	–	–	–	–	–	4.3	2.7	2.0	1.7
Ho	–	–	–	–	–	–	–	–	0.8	0.4	0.4	0.3
Er	–	–	–	–	–	–	–	–	2.3	1.3	1.0	0.9
Tm	–	–	–	–	–	–	–	–	0.4	0.2	0.2	0.2
Yb	1.8	1.4	1.4	1.4	–	–	1.8	1.5	3.6	1.4	1.3	0.9
Lu	0.3	0.2	0.2	0.2	–	–	0.3	0.2	0.5	0.3	0.3	0.2
Sc	45.0	50.0	38.0	47.0	–	–	31.0	29.0	40.8	52.8	35.7	27.7
Cr	353	367	315	255	296	120	29	13	–	–	–	–
Co	41	48	43	41	–	–	30	32	29	22	21	28
Cs	2.0	1.1	0.5	0.5	–	–	0.5	0.5	2.13	0.29	0.71	0.47
Hf	1.4	0.9	0.9	1.1	–	–	1.2	0.8	1.9	1.6	2.4	2.2
Ta	0.23	0.17	0.06	0.2	–	–	0.29	0.13	0.13	0.08	0.11	0.07
Th	0.7	0.61	0.45	0.6	–	–	0.6	0.36	0.25	0.29	0.38	0.37
U	0.7	0.71	0.4	0.6	–	–	0.6	0.4	0.28	0.37	0.30	0.82
Ba	580	390	300	1230	100	800	350	260	593	23	146	265
Rb	9.4	5.7	10.4	31.1	18.5	19.8	16.6	9.2	60.3	1.6	11.9	15.3
Sr	817	335	826	691	201	489	552	711	813	540	776	482
Y	11.3	16.6	9.7	13.1	9.6	17.0	22.4	15.7	27.8	16.7	13.9	11.2
Zr	42	38	29	37	18	41	62	40	71	102	115	127
Nb	2.1	1.3	0.9	2.0	1.0	2.3	4.3	1.8	2.1	1.9	2.4	2.3
Nb/Y	0.18	0.08	0.10	0.16	0.11	0.13	0.19	0.11	0.08	0.11	0.17	0.21
Ba/Rb	62	68	29	40	5	40	21	28	10	14	12	17
Zr/Nb	20	29	31	18	18	18	14	23	34	54	48	55
Al ₂ O ₃ /TiO ₂	20.3	22.7	25.9	25.2	24.7	18.0	30.7	29.9	23.9	23.0	29.9	34.6
Sr/Y	72.34	20.18	85.60	52.75	21.04	28.82	24.64	45.27	29.21	32.39	55.87	42.93
(La/Sm) _n	1.73	1.61	1.22	1.68	–	–	1.48	1.36	0.85	1.22	1.80	1.55
(Gd/Yb) _n	1.32	1.17	1.12	1.41	–	–	1.31	1.22	0.99	1.02	1.52	1.21
(La/Yb) _n	2.51	1.99	1.42	2.63	–	–	2.12	1.81	0.74	1.94	2.54	2.16
(Nb/La) _{pm}	0.31	0.44	0.79	0.35	–	–	0.73	0.44	0.23	1.02	0.35	0.70
(Th/La) _{pm}	0.31	0.56	1.07	0.79	–	–	0.86	0.75	0.93	1.20	0.60	1.57
(Nb/Th) _{pm}	0.99	0.78	0.74	0.44	–	–	0.85	0.59	0.25	0.85	0.59	0.44

Note. Subgroups: high-Mg (1–5) and low-Mg (6–12). * In these samples we analysed the composition of clinopyroxene phenocrysts.

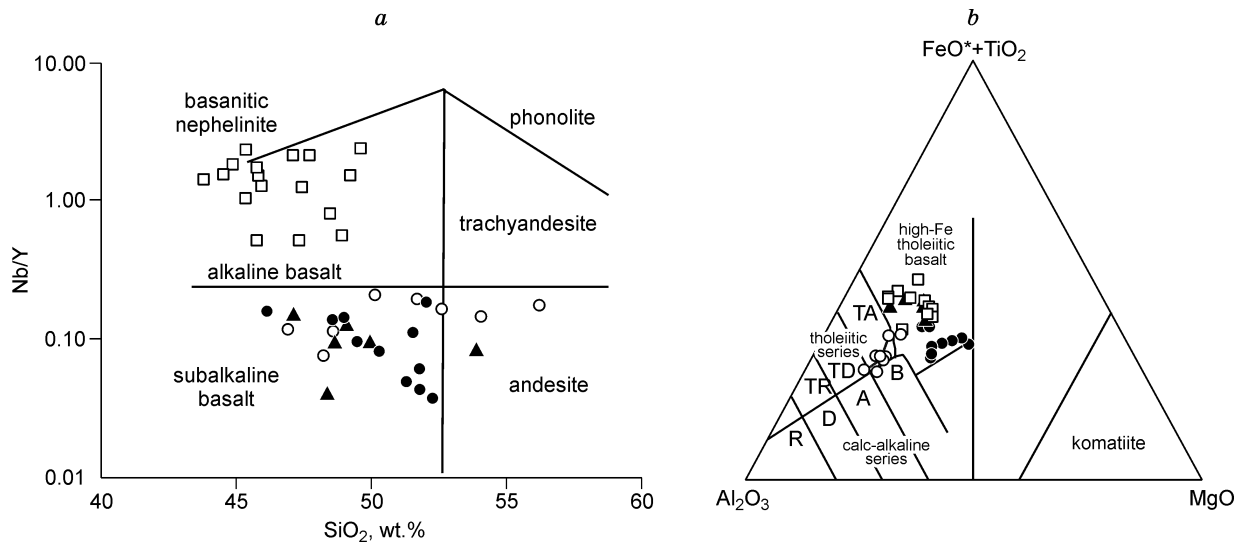


Fig. 4. Classification geochemical diagrams for basalts of the Katun' AC. *a*, Nb/Y vs. SiO₂ (Winchester and Floyd, 1977); *b*, Al₂O₃-FeO*+TiO₂-MgO (Jensen, 1976). Tholeiitic series: TA, andesite; TD, dacite; TR, rhyolite; calc-alkaline series: B, basalt; A, andesite; D, dacite; R, rhyolite. Symbols of basalts: squares, OIB-type; Manzhelok Formation (Group 1); triangles, MORB-type, Group 2; circles, Ust'-Sema Formation, Group 3 (subgroups: solid symbols, high-Mg; open symbols, low-Mg).

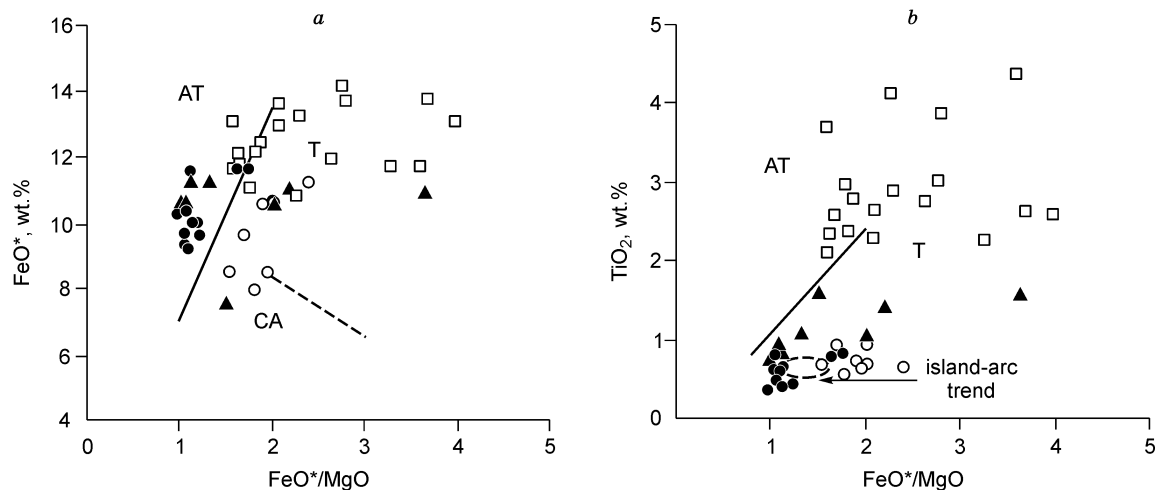


Fig. 5. Bivariate plots: *a*, FeO* vs. FeO*/MgO; *b*, TiO₂ vs. FeO*/MgO. Discriminant fields and trends of abyssal tholeiite (AT), tholeiite (TH), and calc-alkaline volcanic rocks (CA) are after Miyashiro (1973). Symbols as in Fig. 4.

at Mg# = 33–64; Fe₂O₃ = 11.2–15.6, TiO₂ = 0.7–1.5, P₂O₅ = 0.14–0.66, Al₂O₃ = 13.3–16.8 wt.%. With increasing MgO the concentrations of TiO₂, Al₂O₃, and P₂O₅ decrease and those of Nb, Th, Sm and La span narrower intervals (Fig. 6). The wide variations of Ba/Rb (from 34 to 333) indirectly confirm the high mobility of these elements during postmagmatic processes. The Zr/Nb ratios are higher than those in Group 1, and range from 19 to 32 (26 in average). The high-Mg subgroup is characterized by a lower Zr/Nb, but a higher Al₂O₃/TiO₂ ratio (Table 3). Compared to Group 1 high-Ti basalts, the MORB-type volcanic rocks are depleted in Fe₂O₃, P₂O₅, Nb, Zr, La, Sm, and Th (Fig. 6, Table 3) and possess flat REE patterns (Fig. 7, *b*; La_{nav} = 12.4; La/Yb_n = 1.4–2.1) showing low differentiation of LREE and HREE (La/Sm_n =

1.0–1.4; Gd/Yb_n = 1.3–1.6). The multi-element spectra or spider diagrams (Fig. 8, *b*) display Nb negative anomalies relative to La and Th (Nb/La_{pm} = 0.3–0.6; Nb/Th_{pm} = 0.4–0.7). The values of Nb/La_{pm} < 1 are typical of many MORB (Haase, 2002), but those of Nb/Th_{pm} < 1 are not. However, taking into account the old age of basalts, their eruption in oceanic floor setting and the subsequent metamorphism related to accretion processes, we consider the Th enrichment of those relatively LREE-Ti-Nb-depleted basalts a result of hydrothermal alteration and metamorphism.

The basalts of Groups 1 and 2 of the Katun' accretionary wedge (see section “Geological outline...”) have different contents of TiO₂, HFSE, REE and different Zr/Nb ratios (Tables 2, 3). Group 1 high-Ti basalts are characterized by

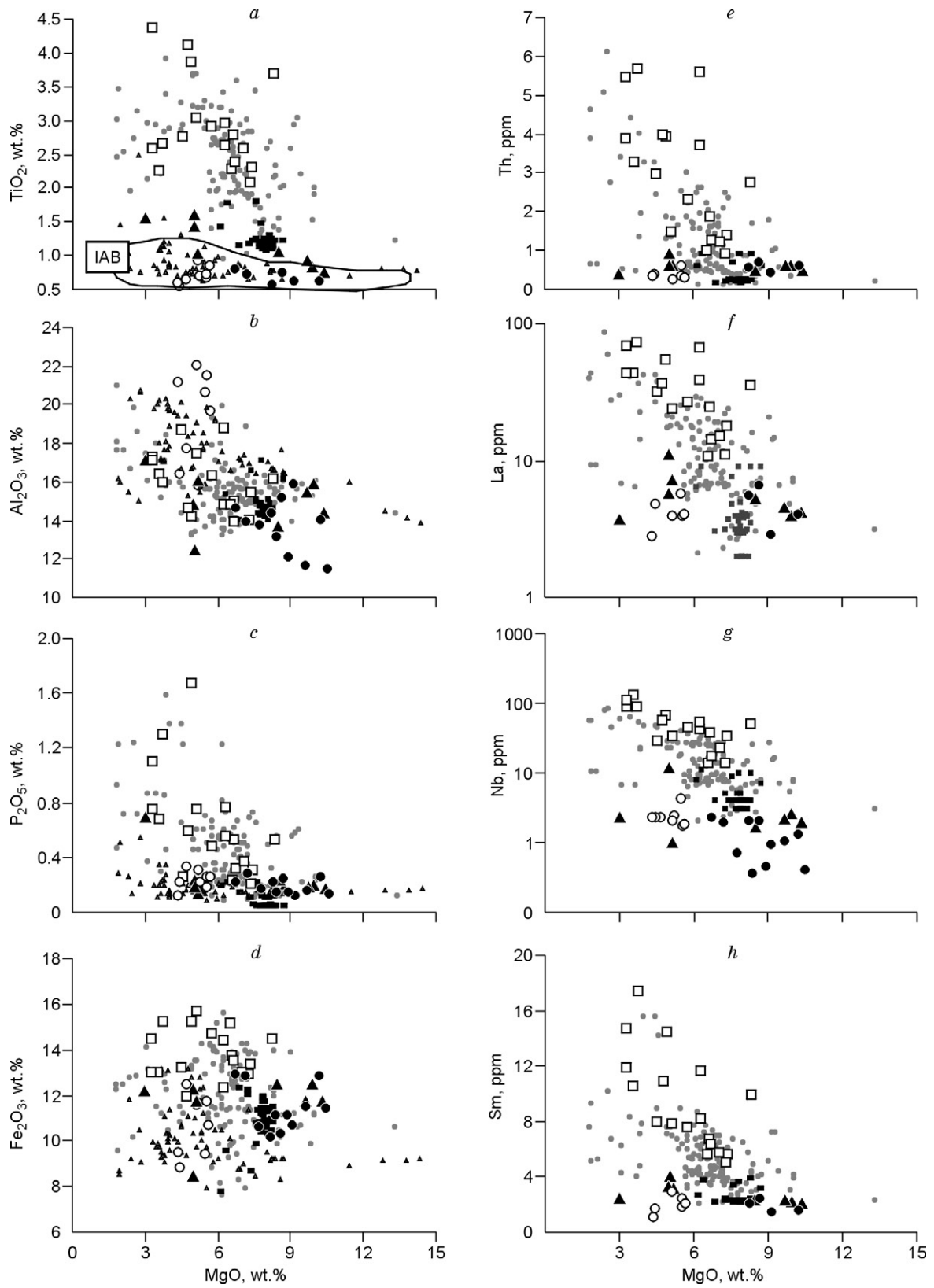


Fig. 6. Binary diagrams of major elements vs. MgO. Small symbols show the compositions of tholeiites of the Emperor–Hawaii Chain of Seamounts (squares) (Regelous et al., 2003), island arcs (triangles), and Western Pacific mid-oceanic ridges (dots) (GEOROC database: <http://georoc.mpch-mainz.gwdg.de>). Other symbols as in Fig. 4.

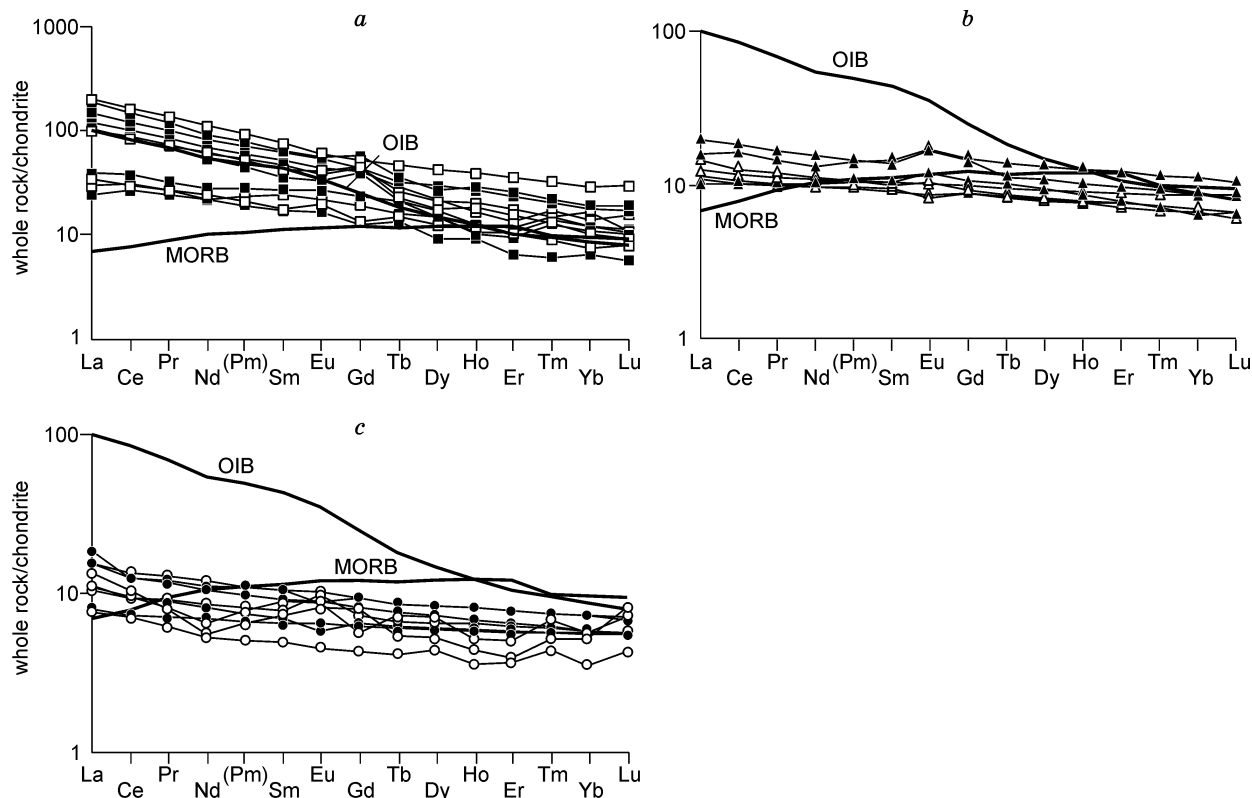


Fig. 7. Chondrite-normalized rare-earth element patterns: *a*, Group 1 (OIB type; Manzhelok Formation); *b*, Group 2 (MORB type); *c*, Group 3 (suprasubduction type, Ust'-Sema Formation). The normalizing values are from (Sun and McDonough, 1989). Symbols of subgroups (MORB-type and Ust'-Sema basalts): light, low-Mg; dark, high-Mg.

enrichment in LREE and HFSE and low Zr/Nb ratios (6.2), i.e., compositionally similar to oceanic island basalts (OIB). Group 2 medium-Ti basalts possess geochemical affinities to N-MORB, because they are depleted in HFSE and LREE and have higher Zr/Nb ratios (26).

Thus, the geochemical features of Group 2 basalts are similar to those of mid-oceanic ridge basalts. In the Edigan site (Dobretsov et al., 2004), they occur in the base of the high-Ti OIB-type basalts of the Manzhelok Formation (Group 1), and this allows us to regard them as fragments of ophiolitic sections of the Paleo-Asian Ocean. Group 1 basalts are compositionally close to alkaline basalts of numerous oceanic islands formed without contamination by crustal material (Frolova and Burikova, 1997; Garcia et al., 1986). They represent intraplate volcanic series erupted in an oceanic island setting related to “hot spot” magmatism (mantle plume).

Middle Cambrian basalts of the Ust'-Sema Formation

Group 3 basalts (Ust'-Sema Formation) have a major and trace-element composition different from that of the Early Cambrian basalts of Group 1 (OIB type), but close to that of Group 2 basalts (MORB-type) except for the contents of TiO₂ and ratios of Al₂O₃/TiO₂, Sr/Y, and Zr/Nb (Table 2–4, Figs. 5, *b* and 6, *a*). Group 3 basalts are characterized by a wide range of Mg# and SiO₂ (44–63 and 45.0–54.2 wt.%, respectively) at a relatively narrow range of Fe₂O₃ (8.5–

12.3 wt.%). The contents of TiO₂ vary from 0.53 to 0.89, P₂O₅ = 0.1–0.28, Al₂O₃ = 13.4–20.6 wt.% (Table 4). Concentrations of Al₂O₃ decrease as Mg# increase (Fig. 6, *b*). In most MgO versus major and trace elements plots Group 3 basalts form either zero trends parallel to the MgO axis (e.g., TiO₂, P₂O₅, Th, Nb, and Sm), or have scattered distribution (e.g., Fe₂O₃ and La) with MgO changing (Fig. 6). Ratios of Zr/Nb vary from 14 to 55 with the average value of 32.6, i.e., higher than those in Groups 1 and 2 with averages of 6.2 and 26, respectively.

We consider two subgroups in Group 3 having different concentrations of MgO (8.8 and 5.2 averages), and Al₂O₃ (14.0 and 19.7 averages; Figs. 4–6). In the binary diagrams shown in Fig. 6, the high-Mg subgroup plots close to MORB, whereas the low-Mg subgroup plots close to the island-arc field. However, the subgroups have similar chondrite normalized REE patterns and consequently ratios of La/Sm_n, Gd/Yb_n and La/Yb_n, and similar primitive-mantle normalized multi-element patterns (Figs. 7, 8; Table 4). The flat REE patterns are similar to those of Group 2, i.e., have a slightly enriched LREE (Figs. 7, *b*, *c*). The mean values of La_n (12.1), La/Yb_n (2.0), La/Sm_n (1.5) and Gd/Yb_n (1.2) are close to those in Group 2 (see previous section). The multi-element spectra of Group 3 (Figs. 8, *b*, *c*) also possess negative Nb anomalies relative to La and Th (Nb/La_{pm} = 0.23–0.79; Nb/Th_{pm} = 0.25–0.99). However, unlike Group 2, several Ust'-Sema samples are characterized by small positive Zr-Hf anomalies

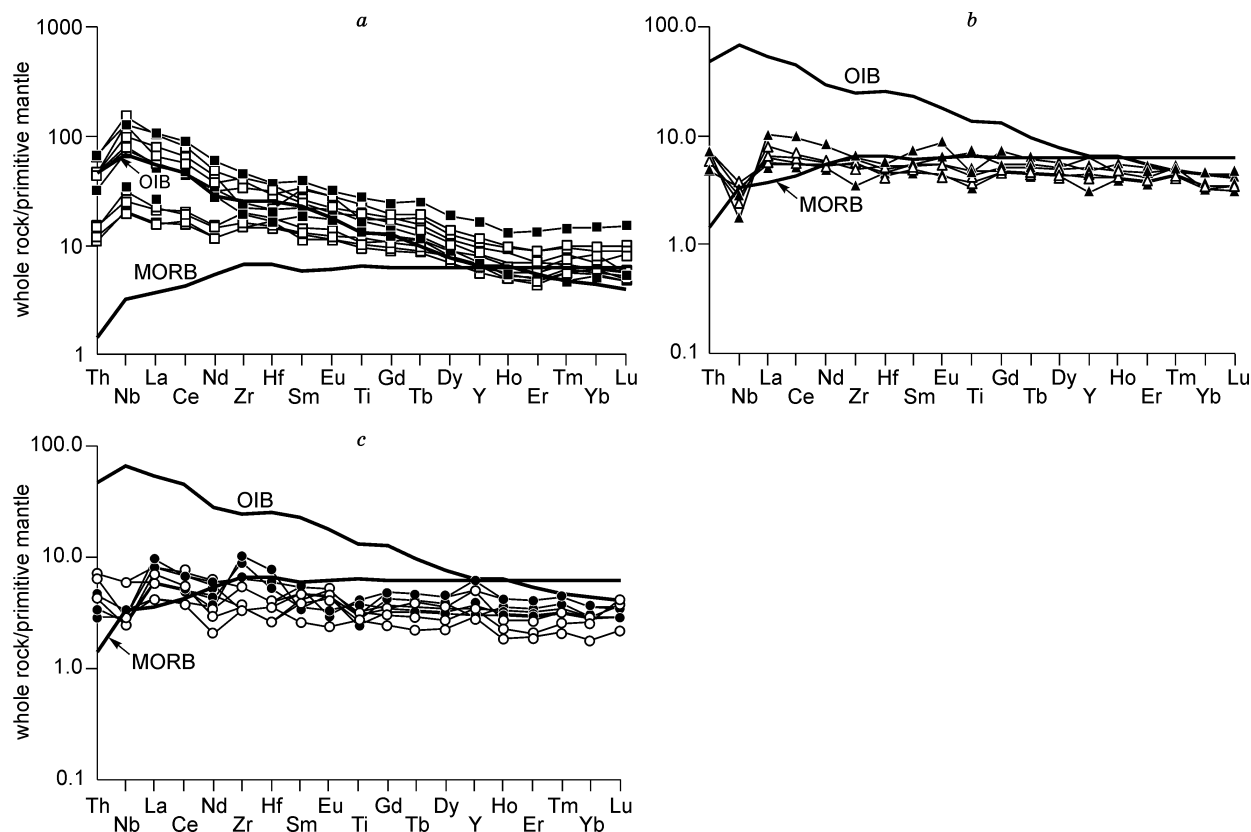


Fig. 8. Primitive mantle-normalized multicomponent diagrams. *a*, Group 1 (OIB type; Manzhelok Formation); *b*, Group 2 (MORB type); *c*, Group 3 (suprasubduction type; Ust'-Sema Formation). The normalizing values, MORB and OIB, are from (Sun and McDonough, 1989). Symbols as in Fig. 7.

(Fig. 8, *c*). Generally, the character of distribution of the major and trace elements suggest their formation in a suprasubduction setting.

Sr and Nd isotopes

Table 5 shows Sr and Nd isotope data for basalts of the Katun' accretionary complex: Group 1 (6 samples) and Group 2 (1 sample). The Sr and Nd isotope ratios were corrected for radioactive decay since the time of their eruption, i.e., 540 Ma, and the ϵ_{Sr} and ϵ_{Nd} values are given relative to BABI and CHUR, respectively. All values of ϵ_{Nd} are positive

and range from +0.9 to +5.2 in Group 1 basalts, i.e., similar to those in lavas of the Emperor–Hawaii Chain of Volcanoes, Cook islands, Galapagos islands and Iceland (Fig. 9) (Ito and Mahoney, 2005; Regelous et al., 2003). The variations of $\epsilon_{Nd}(t)$ in Group 1 basalts of the Katun' AC suggest their heterogeneous mantle source. The wide range of Sr isotopes (I_{Sr}) from 0.70347 to 0.70583 (Fig. 9) suggests either isotopic exchange between Sr-rich sea water and basaltic lava erupted in submarine conditions (Dickin, 1995) or hydrothermal alteration in sea floor conditions and subsequent metamorphism.

Table 5. Nd and Sr isotopes in Manzhelok Formation basalts (OIB type) and in MORB-type basalt (Group 2) of the Katun' AC

Sample	Group	Rb	Sr	$^{87}Rb/^{86}Sr$	$^{87}Sr/^{86}Sr$	$\pm 2\sigma$	$I_{Sr}(540)$	$\epsilon_{Sr}(540)$	Sm	Nd	$^{147}Sm/^{144}Nd$	$^{143}Nd/^{144}Nd$	$\pm 2\sigma$	$\epsilon_{Nd}(0)$	$\epsilon_{Nd}(540)$	La/Sm
242-2	2	8	472	0.016	0.70583	1.5×10^{-5}	0.70571	8.14	3.0	10.8	0.16586	0.51285	0.5×10^{-5}	25.0	6.3	2.2
Kat-34-07	1	3.0	415	0.022	0.70429	4.0×10^{-5}	0.70412	3.68	5.0	15.7	0.22825	0.51280	1.5×10^{-5}	3,7	0,9	2.3
Kat-52-07	1	4.0	581	0.020	0.70366	5.0×10^{-5}	0.70351	-5.02	17.4	79.1	0.15860	0.51269	1.3×10^{-5}	-26.1	3.7	4.2
Kat-55-07	1	9.7	425	0.064	0.70405	6.0×10^{-5}	0.70355	-4.38	5.8	19.7	0.21153	0.51275	1.5×10^{-5}	-2.7	1.2	2.7
92-C-1	1	5.7	97	0.170	0.70478	1.9×10^{-5}	0.70347	-5.84	5.2	20.3	0.15382	0.51275	0.9×10^{-5}	-5.7	5.2	2.4
U48*	1	2.7	195	0.040	0.70410	1.4×10^{-5}	0.70410	-1.05	4.0	14.5	0.16860	0.51276	0.6×10^{-5}	2.3	4.5	2.6
U51*	1	2.8	350	0.023	0.70423	0.9×10^{-5}	0.70423	2.69	4.7	17.5	0.16380	0.51274	0.6×10^{-5}	2.0	4.6	2.5

* From (Utsunomiya et al., 2009).

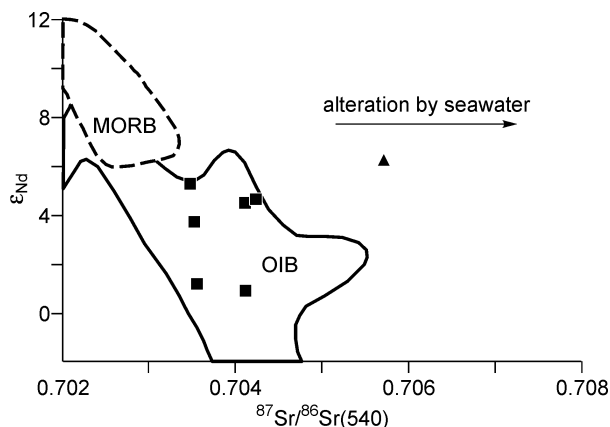


Fig. 9. $\epsilon_{Nd}-^{87}Sr/^{86}Sr$ plot for oceanic basalts of the Katun' AC. The fields for MORB and OIB were modified from (Zindler and Hart, 1986).

In the $\epsilon_{Nd}-^{87}Sr/^{86}Sr$ diagram, the points of Group 1 basalts plot in the field of oceanic islands. The increased values of $^{87}Sr/^{86}Sr$ in the Group 2 sample can be explained by postmagmatic alteration in sea floor conditions. The Manzherok basalts possibly erupted on the surface of the oceanic island or in shallow water conditions, and therefore the effect of sea water was relatively weak. No correlation has been found between the values of isotopic ratios ($^{143}Nd/^{144}Nd$ and $^{87}Sr/^{86}Sr$) and the enrichment in LREE.

Petrogenesis of basalts

PT-conditions of basalt formation

We have calculated the parameters of basalt crystallization based on the composition of clinopyroxene phenocrysts (Table 6). According to the pyroxene thermometer (Lindsley, 1983) (Fig. 3b) the minimal crystallization temperatures of pyroxenes from Ust'-Sema samples C-72g-04 (high-Mg basalt) and C-73a-04 (low-Mg basalt) range from 1050 to 1160 °C and from 1000 to 1100 °C, respectively. The points of sample Kat-55-07 of the Manzherok Formation plot between the isotherms of 1150 and 1200 °C. Besides, we used a software developed by I.V. Ashchepkov et al. (2010) to calculate the petrogenetic parameters based on the monopyroxene thermometers by (Mercier, 1981) and (Nimis and

Taylor, 2000). Our calculated temperatures of crystallization for Manzherok basalts appeared averagely higher than those for Ust'-Sema basalts: 1175 °C and 1097 °C, respectively. The temperature values for the high-Mg Ust'-Sema sample are higher than those for the low-Mg sample: 1147 °C and 1046 °C, respectively (mean values after two thermometers; Table 6). The temperatures were calculated for a fixed pressure of 2 kbar, which probably corresponds to a pressure at the beginning of the basalt melt crystallization in a subsurface intermediate magmatic chamber.

Fractional crystallization

Fowler and Jensen (1989) modeled the evolution of Mg-to Fe-tholeiites of the Abitibi belt: they found that the compositional range could be accounted for by fractional crystallization of olivine, and minor clinopyroxene, plagioclase, and Fe-Ti oxides. The major element composition of Group 2 basalts allows us to suggest an insignificant fractionation of titanomagnetite and plagioclase because MgO increases with decreasing TiO₂ and Al₂O₃, respectively. Fractionation of clinopyroxene was possible in Group 3 basalts, based on a phenocryst assemblage of this mineral (Fig. 2) (Gibsher et al., 1997) and a negative correlation between MgO and Al₂O₃ (Fig. 6).

In terms of trace elements, the wide variations of Mg# in the tholeiitic basalts of Groups 2 and 3 (Tables 3 and 4) could be indicative of a relationship between the Nb anomalies and fractional crystallization, because Nb is compatible in Fe-Ti oxides, which are probable mineral phases fractionating from basaltic melts. However, there is no correlation between concentrations of Nb and TiO₂ (Fe₂O₃) (Fig. 6, a, d) and therefore we do not consider fractionation of Nb by Fe-Ti oxides as a factor of the redistribution of Nb after the formation of an initial basaltic melt. The limited variation of La/Sm_n ratios over a wide range of Mg# (from 30 to 60) contents within Groups 2 or 3 (Tables 2–4) suggest that there was no significant LREE fractionation, and moreover there is no correlation of Nb anomalies with Mg# (Fig. 6, g; Table 7). Consequently, Nb-LREE interelement ratios in the basalts of Groups 2 and 3 are independent of olivine, clinopyroxene, plagioclase, or Fe-Ti oxide fractionation or accumulation.

The MgO versus incompatible element diagrams for the Group 1 basalts suggest that at a glance, their compositional

Table 6. Crystallization temperatures for basalts of the Manzherok and Ust'-Sema Formations of the Katun' AC

Pyroxene monomineral thermometer	Manzherok Formation			Ust'-Sema Formation					
				high-Mg			low-Mg		
	<i>T</i> _{max} , °C	<i>T</i> _{min} , °C	<i>T</i> _{mean} , °C	<i>T</i> _{max} , °C	<i>T</i> _{min} , °C	<i>T</i> _{mean} , °C	<i>T</i> _{max} , °C	<i>T</i> _{min} , °C	<i>T</i> _{mean} , °C
Nimis and Taylor (2000)	1180	1093	1132	1229	1093	1133	1090	1011	1017
Mercier (1981)	1293	1150	1218	1255	1159	1162	1084	907	1076
Lindsley (1983)	1210	1130	1175	1160	1050	1120	1100	1000	1050
Mean on all thermometers	1175, °C			1138, °C			1047, °C		

Table 7. Summary of geological and geochemical features of three groups of basalts of the Katun' AC

Formation (Group)	Manzherok (1)	Eskonga	Ulus-Cherga (2)		Ust'-Sema (3)	
Subgroup	high-Mg (<i>N</i> = 5)	low-Mg (<i>N</i> = 12)	high-Mg (<i>N</i> = 4)	low-Mg (<i>N</i> = 3)	high-Mg (<i>N</i> = 15)	low-Mg (<i>N</i> = 10)
Mode of occurrence	thick lava flows		thin lava flows		several meters thick dikes and flows	
Age	Early Cambrian		Late Neoproterozoic–Early Cambrian		Middle Cambrian	
Associated OPS sediments	Massive carbonates and slope facies		Siliceous and lime mudstone, chert		–	
SiO ₂	47.3	46.4	46.7	50.2	48.5	48.7
TiO ₂	2.3	3.3	0.9	1.4	0.6	0.7
Mg#	50	41	61	45	61	49
Al ₂ O ₃ /TiO ₂	6.2	5.1	17	12.4	25.2	28.3
Zr/Nb	12	5.4	26.5	–	24.5	38
La/Sm _n	1.5	2.5	1.3	1.6	1.6	1.4
Gd/Yb _n	1.7	3.0	1.3	1.4	1.2	1.2
Nb/La _{pm}	1.3	1.4	0.47	0.39	0.47	0.58
Nb/Th _{pm}	1.8	2.1	0.46	0.47	0.73	0.59
Zr*/Zr	1.1	0.9	0.99	1.00	1.4	1.1

Note. Geochemical data are given as mean values. Dash, data on two samples only are available (see Table 3). Zr*/Zr ratios were calculated according to the method from (Taylor and McLennan, 1985).

variations can be accounted for by fractional crystallization (Fig. 6, *a*, *c*, *e–h*). However, the compositional variations basalts cannot be explained by only fractional crystallization. In particular, the Al₂O₃/TiO₂ versus Gd/Yb_n diagram indicates variations of the degree of melting and/or compositional variation of the source mantle (Fig. 10, *a*). On the other hand, the basalts of both Group 2 and Group 3 are characterized by variable Al₂O₃/TiO₂ ratios but similar Gd/Yb_n ratios that are more typical of fractional crystallization.

Degrees of partial melting

OIB-type basalts (Group 1). The variable compositions of both major oxides and incompatible elements in Group 1 basalts suggest different conditions of the partial melting of source mantle during generation of basaltic melts. The basalts of Group 1 are characterized by high degrees of HREE differentiation (Table 2), which suggest partial melting in the garnet stability field. They can be subdivided into two groups based on MgO, REE patterns, incompatible elements and Zr/Nb ratios: LREE-enriched and moderately LREE-enriched groups. (Figs. 7, 8; Table 7). The wide variations of incompatible element ratios (Fig. 10, *a*) and two different types of REE patterns (Fig. 7, *a*) support the variable degree of melting as well as mantle source heterogeneity. In those two subgroups, P₂O₅, La, Sm, Th and Nb decrease with increasing MgO (Fig. 6) suggesting different degrees of partial melting of heterogeneous mantle in the mantle plume column. It was previously shown that the low-degree melting of a heterogeneous mantle plume column, which consists of depleted upper mantle and incompatible element-enriched heterogeneities, may lead to the enrichment of the melt in the incompatible elements because the fusible and incompatible elements-en-

riched heterogeneities, possibly from the lower mantle, are selectively and variedly molten (Regelous et al., 2003; Safonova, 2008). At high degrees of melting, the melt is “diluted” by refractory components of the depleted upper mantle so that the concentrations of incompatible elements decrease.

We imply that the two groups of OIB-type basalts of the Katun' AC represent two oceanic islands of different ages, formed over the oceanic lithosphere of different age and consequently different thickness. At 540 Ma, when the mantle plume column tapped the younger and thinner oceanic lithosphere, more amounts of refractory, incompatible element-depleted materials were melted to produce less enriched OIB-type basalts (Samples 1–3, 11 in Table 2). Later, the incompatible elements-enriched basalts of Group 1 (samples 4–10, 12 in Table 2) were formed under the more mature and thicker oceanic lithosphere at about 520 Ma. The degree of melting was lower so that the melt contained higher concentrations of incompatible elements at the expense of more fusible material of mantle plume column heterogeneities.

The variable isotope composition of the basalts also supports a mixing of melts produced by two types of mantle sources: MORB-type depleted refractory upper mantle material and OIB-type enriched fusible mantle material (Fig. 9). A similar scenario was reported for the Emperor–Hawaii Chain of Seamounts and other chains of volcanoes formed in relation to hot spot magmatism (Regelous et al., 2003 and references therein). Besides, our model is supported by the occurrence of these two groups of basalts on different structural levels of the Katun' AC: the more incompatible element enriched basalts were taken in the Edigan site, which is the younger or upper level of the Katun' AC of Early Cambrian age; the less enriched basalts were sampled at the Cheposh and Cherga site,

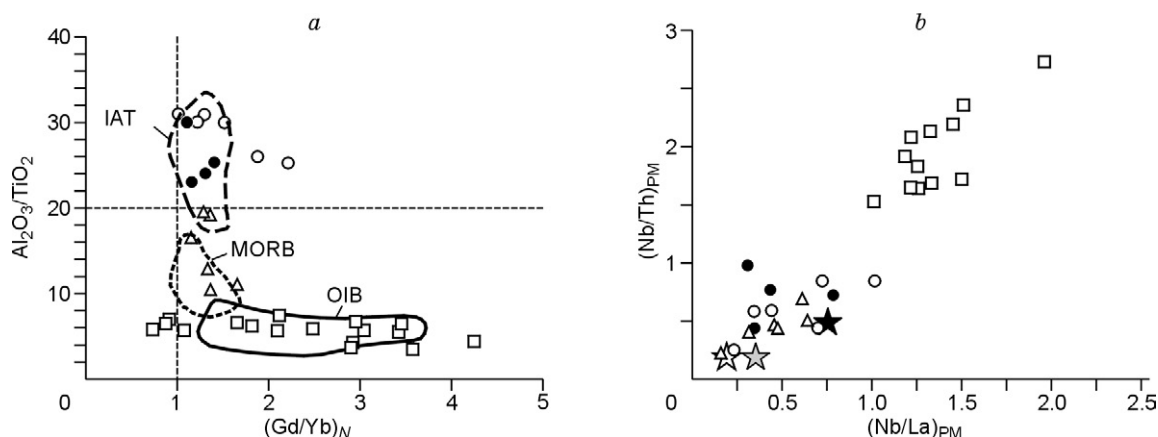


Fig. 10. $\text{Al}_2\text{O}_3/\text{TiO}_2$ ratio vs. Gd/Yb_N (a) and $\text{Nb}/\text{La}_{\text{PM}}$ vs. $\text{Nb}/\text{Th}_{\text{PM}}$ (b) plots indicating variable degrees of melting (Gd/Yb_N), fractional crystallization ($\text{Al}_2\text{O}_3/\text{TiO}_2$), crustal contamination ($\text{Nb}/\text{Th}_{\text{PM}}$) and different mantle sources (Gd/Yb_N , $\text{Nb}/\text{La}_{\text{PM}}$). The fields of the Hawaiian hot spot (OIB), Western Pacific ridges (MORB), and Aleutian island arc (IAT) are shown for comparison. The data on the Aleutian arc are from the GEOROC database (www.georoc.mpch-mainz.gwdg.de/georoc). OIB and MORB, from (Sun and McDonough, 1989).

which are dominated by Late Neoproterozoic–Early Cambrian units of OPS (Fig. 1).

Basalts of Groups 2 and 3. The basalts of Groups 2 and 3 are characterized by close concentrations of REE, Nb and Th, almost flat REE patterns and by the presence of Nb negative anomalies relative to La and Th in the multi-element diagrams (Figs. 7 and 8). Their similar Gd/Yb_N ratios (Fig. 10, a) suggest a similar depth/type of mantle source, which produced the basaltic melts. Those melts obviously experienced no crystallization in intermediate chambers *en route* to the surface as a result of their rapid ascending in a spreading zone. The proportions of major oxides (Fig. 10, b) also suggest similar degrees of melting in a mantle source, although indirectly. The basalts of Groups 2 and 3 are generally depleted in LREE, Nb and Ti and, probably, crystallized from melts formed under relatively high degrees of melting, which are typical of MORB-type mantle sources (DMM) (Saunders et al., 1988).

Mantle sources

The basalts of Group 1 (Manzherok Formation), which are enriched in LREE, Ti and Nb contents, were probably related to a mantle plume or hot spot (Figs. 8 and 10, b; Hofmann, 1997). It is well known that plume-related basalts are enriched in Nb (e.g., Sun and McDonough, 1989). Saunders et al. (1988) supposed that Nb resides in the subducting oceanic slab, whereas LREE and Th are extracted from it to the subarc mantle. Nb can be fractionated from Th and LREE through subduction-induced dehydration, and accumulate through the mixing of subducted oceanic slabs back into the lower mantle, possibly reaching the core-mantle boundary (Brenan et al., 1994; McCulloch and Gamble, 1991).

The majority of Group 1 basalts are characterized by a relatively high degree of REE fractionation (Tables 2 and 7; Fig. 7). Their high Gd/Yb_N ratios are also indicative of garnet fractionation at the formation (>60 km), because the HREE

are partially coherent in garnet (Hirschmann and Stolper, 1996). For these basalts, we suggest plume-related mantle sources melted at depths of the spinel ($\text{Gd}/\text{Yb}_N < 2$) and garnet ($\text{Gd}/\text{Yb}_N > 2$) facies.

The presence of two subgroups in OIB-type basalts, which are characterized by different concentrations and ratios of LREE, Th and Nb (see section “Degrees of partial melting”), is suggestive of a heterogeneous mantle plume source consisting of a column of incompatible element depleted upper mantle material and its hosted incompatible element enriched mantle heterogeneities. Such a mantle source could produce basaltic melts variably enriched in incompatible elements according to the degree of melting and/or the thickness of the overlying oceanic lithosphere (Ito and Mahoney, 2005; Regelous et al., 2003 and the references cited therein; Safonova, 2008) (see also section “Degrees of partial melting”).

The basalts of Groups 2 and 3 are of special interest because they have different structural positions and ages (see section “Geological position...”) and different petrographic and mineralogical features (see section “Petrography and mineralogy”), but close concentrations of both major (except for TiO_2) and trace elements (Table 7). Both Groups 2 and 3 include two subgroups: high- and low-Mg. But the subgroups of MORB-type (Group 2) have different concentrations of TiO_2 (Fig. 6, a), whereas the subgroups of the Ust’-Sema Formation (Group 3) are characterized by different Al_2O_3 (Figs. 6, b and 10, a). On the other hand, all basaltic varieties of both groups are characterized by very close concentrations and ratios of incompatible trace elements (Figs. 6–8, 10). We suggest that those basalts formed from a spinel facies mantle source (see section “Degrees of partial melting”), because the REE patterns of the basalts of both groups display no fractionation of the HREE (Figs. 7, b, c) (Hirschmann and Stolper, 1996) and both groups have similar Gd/Yb_N ratios (Table 3, 4; Figs. 7 and 10, a). The low degrees of LREE differentiation and the negative Nb anomalies (Figs. 7, 8, and 10, b) suggest a similar DMM-type mantle. Although modern

MORBs are characterized by a progressive decrease of concentrations from Sm to La in the REE patterns and from Nb to Th in the multielements patterns (Figs. 7 and 8), the ratio of $(La/Sm)_n$ in Group 2 basalts is slightly higher than 1 (1.2), i.e., they probably formed from a depleted upper mantle source. In Group 3 basalts, the $(La/Sm)_n$ ratios are higher (1.45), which are, combined with other geochemical features, more typical of suprasubduction mantle sources.

The high-Mg basalts of Group 2 (see section “Geochemistry”) are the closest to “classic” MORB, i.e., formed under decompressional melting of the upper mantle (Figs. 6 and 7). We attribute the insignificant enrichment in La and Ce to the influence of a nearby located mantle plume or to the suprasubduction mantle.

The low-Mg basalts of Group 2 are more differentiated and have higher SiO_2 and TiO_2 . The La/Sm_n , Gd/Yb_n , Nb/La_{pm} and Nb/Th_{pm} ratios are close to those in the high-Mg varieties, suggesting a similar mantle source (Table 7). We propose that they formed at the beginning of the oceanic ridge subduction: the basalts could not erupt on the surface right after the melting, like in a typical spreading zone, but “delayed” in an intermediate chamber. Thus, the low-Mg basalts of Group 2 formed from a similar MORB-type mantle source, like the high-Mg basalts of the same group, however the subduction of oceanic ridge resulted in the differentiation of the melt, possibly due to plagioclase crystallization, and therefore its insignificant enrichment in SiO_2 and TiO_2 . On the other hand, we must admit that a “simple” differentiation of the melt in an intermediate chamber, without any relation of ridge subduction, could give a similar result.

Both the MORB-type basalts and the low-Mg basalts of the Ust'-Sema Formation probably formed from a DMM-type source. Both groups are geochemically similar (Figs. 6–9), although the Ust'-Sema basalts contain more Al_2O_3 and less TiO_2 (Fig. 10, a). In Group 3, the low-Mg basalts possibly did not experience plagioclase fractionation because they have higher Al_2O_3 contents than the low-Mg ones (Fig. 6, b).

According to experimental data, high-Mg island-arc tholeiites can be melted near the volcanic front at mantle depths close to the mantle-crust boundary (Kushiro, 1984; Tatsumi, 1991). Therefore, we suggest that the high-Mg Ust'-Sema basalts ($Gd/Yb_n = 1.2$; $Mg\#_{av.} = 61$; Table 4) possibly formed in mantle wedge, i.e., in suprasubduction conditions, as a result of the melting of subducted oceanic slab. More evidence for such a high-temperature mantle source for the high-Mg basalts of the Ust'-Sema Formation comes from the above estimated of crystallization temperatures (see section “PT-conditions” and Table 6).

Geodynamic model

We propose the following geodynamic model for the formation of the volcanic rocks of the Katun' accretionary complex (Fig. 11).

In the Late Neoproterozoic–Early Cambrian, the oceanic crust, i.e., the MORB-type basalts of Group 2, formed in

spreading zones. That oceanic crust of the Paleo-Asian Ocean subducted beneath the active margin of the Siberian continent, which evolved likewise the present-day Western Pacific. The subduction resulted in formation of the primitive island arc (Buslov and Watanabe, 1996; Buslov et al., 1993, 2001; Simonov et al., 2004) (Fig. 11, a).

In the Early Cambrian, plume-related activity in the Paleo-Asian Ocean formed islands and/or seamounts, i.e., the Manzherok Formation basalts of Group 1. During the subduction, those oceanic seamounts were accreted to the primitive island arc and later, together with the fragments of MORB-type oceanic lithosphere and OPS, incorporated into the accretionary complex (Fig. 11, b). The normal island arc was formed by the end of the Early Cambrian (Buslov et al., 2002).

By the beginning of the Middle Cambrian, the spreading zone met the subduction zone and started to submerge. This resulted in the change of the composition of the melts, which were produced by a DMM-type mantle source, and formation of low-Mg basalts of Group 2, extension structures in the accretionary wedge (Polat et al., 1998), and intrusion of thick parallel dikes of the Ust'-Sema Formation (Fig. 11, c).

The submergence of hydrated rocks of the oceanic crust into the subduction zone resulted in increased oxygen fugacity, origination of higher temperature basaltic melts at the crust-mantle boundary and formation of the high-Mg basalts and andesibasalts of the Ust'-Sema Formation in a suprasubduction setting. Those volcanics are characterized by island-arc geochemical signatures, i.e., low Ti, $La/Nb_{pm} < Th/Nb_{pm}$, $La/Sm_n = 1.3$, inherited from the subarc mantle or mantle wedge, through which their parental basaltic melts ascended to the surface.

We can prove the ridge subduction model by the following facts: (1) the occurrence of the complex of subvertical and subparallel basaltic dikes (Ust'-Sema Formation) over a distance of more than 200 km; (2) the dikes cut the accretionary complex (Buslov et al., 1993; Dobretsov et al., 2004); (3) the chemical composition of Ust'-Sema basalts is similar to MORB but depleted in Ti due to titanomagnetite fractionation from the DMM-type basaltic melt; (4) high temperatures of crystallization of the suprasubduction basalts of the Ust'-Sema Formation (Table 6); (5) occurrence of adakite-like basaltic varieties in the dikes of the Ust'-Sema Formation (samples T4006, T4017, T4044; Table 4), which are characterized by increased concentrations of MgO (8.3–9.8 wt.%) and Sr (690–820 ppm) and decreased Y (9–13 ppm) (Lytwyn et al., 2000). The latter, in combination with the occurrence of adakite-like rocks within the area of the Kuznetsk–Altai island arc and occurrence of Early Cambrian (Sarakokshinsky massif; 5126 Ma) (Kruk et al., 2007) and Late Cambrian granites in the frontal zone of subduction, i.e., in Gorny Altai and Kuznetsk Alatau (Nalivkin, 1983; Shokalsky et al., 2000; unpublished data—courtesy of G.A. Babin), is indicative of a “slab window”, which is a major result of ridge subduction (Thorkelson, 1994). Similar geological complexes, which formed during the subduction of the mid-oceanic ridge separating the reconstructed Kula and Farallon

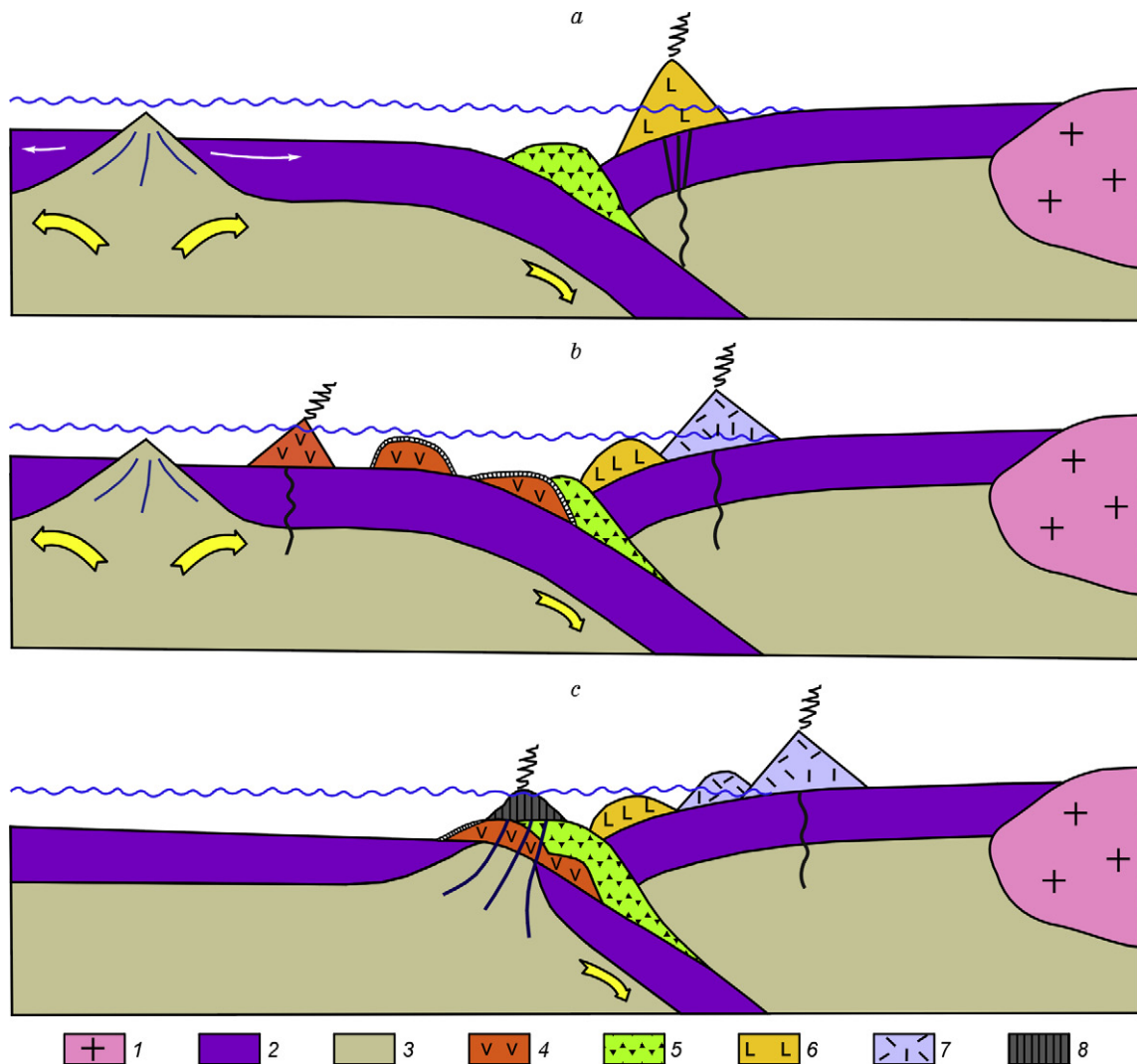


Fig. 11. A geodynamic model for the formation of basalts of the Katun' accretionary complex, Gorny Altai. *a*, Late Neoproterozoic: formation of the oceanic crust of the Paleo-Asian Ocean in spreading zones (Group 2, MORB-type basalts) and its subduction beneath the Kuznetsk–Altai island arc at the margin of the Siberian continent; formation of the primitive island arc. *b*, Early Cambrian: formation of oceanic islands in relation to mantle plume activity (Group 1, OIB-type basalts of the Manzherek Formation) and their accretion to the primitive arc, together with the oceanic crust; formation of the normal island arc. *c*, Middle Cambrian: ridge subduction, formation of the Ust'-Sema Formation—intrusion of parallel dikes and the eruption of basaltic lavas. 1, Siberian continent; 2, oceanic crust (MORB); 3, upper mantle; 4, oceanic islands/seamounts; 5, accretionary complex; 6, primitive island arc; 7, normal island arc; 8, suprasubduction volcanic units.

oceanic plates, were described in Southern Alaska (Lytwyn et al., 1997, 2000).

On the other hand, the wide occurrence of Early Paleozoic picrite-bearing ultramafic-mafic rock assemblages (Borodina et al., 2004; Izokh et al., 2006, 2010) and carbonatites (Vrublevskii et al., 2009), is suggestive of a large, possibly plume-related, magmatic event superimposed onto the accretionary complex, under which the ridge subducted. The proposed relation of the placer platinum deposits in the neighbouring Mongolian Altai to the Ureg Nuur picrite-basaltic complex, which is a probable analogue of the Ust'-Sema Formation (Izokh et al., 2010), indirectly supports the possible participation of a mantle plume in the formation of the Gorny Altai picrites and diopside-rich basalts.

Generally speaking, some key elements such as Ti, LREE, and Nb contents are variably more abundant in plume-related

magmas formed in an intraoceanic (Hawaii, Iceland, and Ontong-Java) or continental (Siberian, Emeishan and Kuzbass Traps and volcanoes of the Minusa basin, Vitim plateau and Central Mongolia) settings, and at modern active margins (Jeju Island, South Korea, and the SW part of Japan Sea) (e.g., Ali et al., 2005; Buslov et al., 2010; Hawkesworth et al., 1995; Hofmann, 1997; Regelous et al., 2003; Sheth and Melluso, 2008; Tatsumi et al., 2005; Zolotukhin and Al'mukhamedov, 1988). The absence of geochemical and geophysical (lithosphere thickening) signatures of mantle plumes is inconsistent with the plume model.

More evidence for the proposed model of ridge subduction or the alternative mantle plume model may come from the isotopic study of Ust'-Sema basalts and a more detailed and extensive study of trace-element and isotopic compositions of volcanic and igneous rocks of the western Altai–Sayan area.

Conclusions

The paper presents results of our comprehensive study of the Late Neoproterozoic–Middle Cambrian basaltic rocks of the Katun' accretionary complex from the northern Russian Altai (southwestern Siberia), which includes the detailed analysis of their chemical composition (major and trace elements, Sr and Nd isotopes) and petrologic conditions of crystallization of basaltic melts (monomineral thermometry). Based on the whole geological, stratigraphic, petrologic and geochemical data, we concluded the following.

1. Three groups of mafic volcanic rocks, with the Late Neoproterozoic to Middle Cambrian age and different structural position, coexist in the Katun' accretionary complex.

2. The Late Neoproterozoic–Early Cambrian oceanic basalts were formed in an oceanic ridge setting, evident in their association with oceanic siliceous sediments, medium TiO₂ and Zr/Nb ratio (~26), flat REE patterns and Nb/La_{pm} ratios < 1. There are high-Mg and low-Mg varieties of basalts characterized by different degrees of differentiation (SiO₂, TiO₂, and MgO). These two varieties formed in a “normal” mid-oceanic ridge and ridge subduction settings, respectively.

3. The Early Cambrian basalts of the Manzherok Fm. formed in an oceanic island setting related to mantle plume (hot spot), evident in their association with siliceous-carbonate brecciated sediments of slope facies and limestones of an oceanic island, relatively high crystallization temperatures (1175 °C), enrichment in incompatible elements, high Gd/Yb_{pm}, Nb/Th_{pm}, and Nb/La_{pm} ratios, medium ε_{Nd}, and low Zr/Nb ratio (~9). The wide variations of incompatible elements suggest a variable degree of partial melting of the heterogeneous enriched mantle plume in the spinel (Gd/Yb_n < 2) and garnet (Gd/Yb_n > 2) stability fields.

4. We present the first geochemical data on the suprasubduction basalts of the Ust'-Sema Formation (Middle Cambrian), which are compositionally transitional between MORB and island-arc tholeiites. Both high-Mg and low-Mg subgroups are characterized by low TiO₂, Nb and LREE contents and high Zr/Nb ratio (>25). We suggest that the low-Mg basalts of the Ust'-Sema Formation formed from the same mantle source as the Late Neoproterozoic–Early Cambrian low-Mg oceanic floor basalts, i.e., during ridge subduction and its related rifting of the accretionary complex. The high-Mg basalts of the Ust'-Sema Formation formed during melting of a mantle source located close to the crust-mantle in a suprasubduction setting.

Acknowledgments

The authors would like to express their gratitude to reviewers Olga Turkina and Nikolai Kruk, whose thoughtful analysis and constructive criticism which allowed us to improve significantly the manuscript. Also, we thank our colleagues who determined the concentrations of major and trace elements and isotopes: V.A. Bobrov, V.S. Parkhomenko, Yu.P. Kolmogotov, S.V. Palesskiy, N.M. Glukhova (all from

IGM SB RAS) and Yu.A. Kostitsyn (GEOHI RAS), as well as to A.S. Gibsher (IGM SB RAS) for fruitful discussions. The work was supported by IGM SB RAS grant 9.21 “Geodynamic processes in subduction zones: thermophysical (experimental and theoretical) modeling and comparison with geological and geophysical data” and Academician Dobretsov Scientific School grant no. 65804.2010.5. Inna Safonova is grateful to the Korean Federation of Science and Technology (KOFST), in particular to Dr. Juyong Kim for support during the final stage of the manuscript preparation.

References

- Ali, J.R., Thompson, G.M., Zhou M.-F., Song, X., 2005. Emeishan large igneous province, SW China. *Lithos* 79, 475–489.
- Ashchepkov, I.V., Pokhilenko, N.P., Vladykin, N.V., Logvinova, A.M., Afanasiev, V.P., Pokhilenko, L.N., Kuligin, S.S., Malygina, E.V., Alymova, N.A., Kostrovitsky, S.I., Rotman, A.Y., Mityukhin, S.I., Karpenko, M.A., Stegnitsky, Yu.B., Khmelnikova, O.S., 2010. Structure and evolution of the lithospheric mantle beneath Siberian craton, thermobarometric study. *Tectonophysics* 485 (1–4), 17–41.
- Bednarz, U., Schmincke, H.-U., 1989. Mass transfer during sub-seafloor alteration of the upper Troodos crust (Cyprus). *Contrib. Mineral. Petrol.* 102, 93–101.
- Berzin, N.A., Coleman, R.G., Dobretsov, N.L., Zonenshain, L.P., Xiao Xuchang, Chang, E.Z., 1994. Geodynamic map of the western part of the Paleasian Ocean. *Geologiya i Geofizika (Russian Geology and Geophysics)* 35 (7–8), 8–28 (5–22).
- Bobrov, V.A., Kalugin, I.A., Phedorin, M.A., 1998. SR XFA of element composition of bottom sediments from Teletskoye Lake. *Nucl. Instrum. Methods Phys. Res. A* 405, 569–571.
- Borodina, E.V., Egorova, V.V., Izokh, A.E., 2004. Petrology of Ordovician collision-related layered peridotite-gabbro intrusions (*exemplified by the Mazhalyk intrusion, Southeastern Tuva*). *Geologiya i Geofizika (Russian Geology and Geophysics)* 45 (9), 1075–1091 (1025–1042).
- Brenan, J.M., Shaw, H.F., Phinney, D.L., Ryerson, F.J., 1994. Rutile-aqueous fluid partitioning of Nb, Ta, Hf, Zr, U and Th: implications for high-field strength element depletions in islandarc basalts. *Earth Planet. Sci. Lett.* 128, 327–339.
- Buslov, M.M., 1992. Tectonic nappes of Gorny Altai [in Russian]. Nauka, Novosibirsk.
- Buslov, M.M., Watanabe, T., 1996. Intrasubduction collision and its role in the evolution of an accretionary wedge: the Kurai Zone of Gorny Altai (*Central Asia*). *Geologiya i Geofizika (Russian Geology and Geophysics)* 37 (1), 82–93 (74–84).
- Buslov, M.M., Berzin, N.A., Dobretsov, N.L., Simonov, V.A., 1993. *Geology and Tectonics of Gorny Altai*. UIGGM, Novosibirsk.
- Buslov, M.M., Safonova, I.Yu., Watanabe, T., Obut, O.T., Fujiwara, Y., Iwata, K., Semakov, N.N., Sugai, Y., Smirnova, L.V., Kazansky, A.Yu., Itaya, T., 2001. Evolution of the Paleo-Asian Ocean (Altai–Sayan Region, Central Asia) and collision of possible Gondwana-derived terranes with the southern marginal part of the Siberian continent. *Geosci. J.* 5 (3), 203–224.
- Buslov, M.M., Watanabe, T., Safonova, I.Yu., Iwata, K., Travin, A., Akiyama, M., 2002. A Vendian–Cambrian island arc system of the Siberian continent in Gorny Altai (Russia, Central Asia). *Gondwana Research* 5, 781–800.
- Buslov, M.M., Watanabe, T., Smirnova, L.V., Fujiwara, I., Iwata, K., de Grave, J., Semakov, N.N., Travin, A.V., Kir'yanova, A.P., Kokh, D.A., 2003. Role of strike-slip faulting in Late Paleozoic–Early Mesozoic tectonics and geodynamics of the Altai-Sayan and East Kazakhstan regions. *Geologiya i Geofizika (Russian Geology and Geophysics)* 44 (1–2), 49–75 (47–71).

- Buslov, M.M., Safonova, I.Yu., Fedoseev, G.S., Reichow, M.K., Davies, K., Babin, G.A., 2010. Permo-Triassic plume magmatism of the Kuznetsk Basin, Central Asia: geology, geochronology, and geochemistry. *Russian Geology and Geophysics (Geologiya i Geofizika)* 51 (9), 1021–1036 (1310–1328).
- Defant, M.J., Drummond, M.S., 1990. Derivation of some modern arc magmas by melting of young subducted lithosphere. *Nature* 347, 662–665.
- Dickin, A.P., 1995. *Radiogenic Isotope Geology*. Cambridge University Press, Cambridge.
- Dobretsov, N.L., Berzin, N.A., Buslov, M.M., 1995. Opening and tectonic evolution of the Paleo-Asian Ocean. *Int. Geol. Rev.* 37, 335–360.
- Dobretsov, N.L., Buslov, M.M., Vernikovskiy, V.A., 2003. Neoproterozoic to Early Ordovician evolution of the Paleo-Asian Ocean: implications to the break-up of Rodinia. *Gondw. Res.* 6, 143–159.
- Dobretsov, N.L., Buslov, M.M., Safonova, I.Yu., Kokh, D.A., 2004. Fragments of oceanic islands in the Kurai and Katun' accretionary wedges of Gorny Altai. *Geologiya i Geofizika (Russian Geology and Geophysics)* 45 (12), 1381–1403 (1325–1348).
- Floyd, P.A., Winchester, J.A., 1975. Magma-type and tectonic setting discrimination using immobile elements. *Earth Planet. Sci. Lett.* 27, 211–218.
- Fowler, A.D., Jensen, L.S., 1989. Quantitative trace element modeling of the crystallization history of the Kinojevis and Blake River groups, Abitibi greenstone belt, Ontario. *Can. J. Earth Sci.* 26, 1356–1365.
- Frolova, T.I., Burikova, I.A., 1997. Magmatic formations in Modern Geotectonic Environments [in Russian]. Moscow Univ. Press, Moscow.
- Garcia, M.O., Frey, F.A., Grooms, D.G., 1986. Petrology of volcanic rocks from Kaula Island, Hawaii: implications for the origin of Hawaiian protoliths. *Contrib. Mineral. Petrol.* 94, 461–471.
- Gelinas, L., Mellinger, M., Trudel, P., 1982. Archean mafic metavolcanics from the Rouyn-Noranda district, Abitibi greenstone belt, Quebec. I. Mobility of the major elements. *Can. J. Earth Sci.* 19, 2258–2275.
- Gibsher, A.S., Esin, S.V., Izokh, A.E., Kireev, A.D., Petrova, T.V., 1997. Cambrian diopside-bearing basalts of the Cheposh zone in Gorny Altai: a model for fractionation of hybrid magmas in intermediate magmatic chambers. *Geologiya i Geofizika (Russian Geology and Geophysics)* 38 (11), 1760–1773 (1789–1801).
- Gordienko, I.V., Filimonov, A.V., Minina, O.R., Gornova, M.A., Medvedev, A.Ya., Klimuk, V.S., Elbaev, A.L., Tomurtogoo, O., 2007. Dzhida island-arc system in the Paleozoic Ocean: structure and main stages of Vendian–Paleozoic geodynamic evolution. *Russian Geology and Geophysics (Geologiya i Geofizika)* 48 (1), 91–106 (120–140).
- Gusev, N.I., 1991. Reconstruction of geodynamic regimes for Precambrian and Cambrian volcanism in southeastern Gorny Altai, in: Kuznetsov, P.P. et al. (Eds.), *Paleogeodynamics and formation of mineral-rich zones in South Siberia* [in Russian]. OIGGM SO AN SSSR, Novosibirsk, pp. 32–54.
- Haase, K.M., 2002. Geochemical constraints on magma sources and mixing processes in Easter Microplate MORB (SE Pacific): a case study of plume-ridge interaction. *Chem. Geol.* 182, 335–355.
- Hart, S.R., Hauri, E.H., Oschmann, L.A., Whitehead, J.A., 1992. Mantle plumes and entrainment: isotopic evidence. *Science* 256 (5056), 517–520.
- Hawkesworth, C.J., Lightfoot, P.C., Fedorenko, V.A., Blake, S., Naldrett, A.J., Doherty, W., Gorbachev, N.S., 1995. Magma differentiation and mineralization in the Siberian continental flood basalts. *Lithos* 34, 61–88.
- Hemond, C., Arndt, N.T., Lichtenstein, U., Hofmann, A. W., Oskarsson, N., Steinthorsson, S., 1993. The heterogeneous Iceland plume: Nd–Sr–O isotope and trace element constraints. *J. Geophys. Res.* 98, 15,833–15,850.
- Hirschmann, M.M., Stolper, E.M., 1996. A possible role for garnet pyroxenite in the origin of the “garnet signature” in MORB. *Contrib. Mineral. Petrol.* 124, 185–208.
- Hofmann, A.W., 1997. Mantle geochemistry: the message from oceanic volcanism. *Nature* 385, 219–229.
- Humphris, S.E., Thompson, G., 1978. Hydrothermal alteration of oceanic basalts by seawater. *Geochim. Cosmochim. Acta* 42, 107–125.
- Isozaki, Y., Maruyama, S., Fukuoka, F., 1990. Accreted oceanic materials in Japan. *Tectonophysics* 181, 179–205.
- Ito, G., Mahoney, J.J., 2005. Flow and melting of a heterogeneous mantle. 2. Implications for a chemically non-layered mantle. *Earth Planet. Sci. Lett.* 230, 47–63.
- Izokh, A.E., Vishnevskii, A.V., Polyakov, G.V., Kalugin, V.M., Oyunchimeg, T., Shelepaev, R.A., Egorova, V.V., 2010. The Ureg Nuur Pt-bearing volcanoplutonic picrite–basalt association in the Mongolian Altay as evidence for a Cambrian–Ordovician Large Igneous Province. *Russian Geology and Geophysics (Geologiya i Geofizika)* 51 (5), 521–533 (665–681).
- Jenner, G.A., Longerich, H.P., Jackson, S.E., Fryer, B.J., 1990. ICP-MS—a powerful tool for high precision trace element analysis in earth sciences: evidence from analysis of selected U.S.G.S. reference samples. *Chem. Geol.* 83, 133–148.
- Jensen, L.S., 1976. A New Cation Plot for Classifying Subalkalic Volcanic Rocks. Ontario Division Mines Miscellaneous Paper 66.
- Kerrick, R., Wyman, D., 1997. A Review of developments in trace-element fingerprinting of geodynamic settings and their implications for mineral exploration. *Austral. J. Earth Sci.* 44, 465–487.
- Komiya, T., Maruyama, S., Hirata, T., Nohda, S., 2002. Petrology and Geochemistry of MORB and OIB in the Mid-Archean North Pole region, Pilbara craton, Western Australia: Implications for the composition and temperature of the upper mantle at 3.5 Ga. *Int. Geol. Rev.* 44, 988–1016.
- Komiya, T., Maruyama, S., Hirata, T., Yurimoto, H., Nohda, S., 2004. Geochemistry of the oldest MORB and OIB in the Isua Supracrustal Belt, Southern West Greenland: Implication for the composition and temperature of early Archean upper mantle. *The Island Arc* 13, 47–72.
- Kruk, N.N., Rudnev, S.N., Shokalsky, S.P., Babin, G.A., Kuibida, M.L., Lepekhnina, E.N., Kovach, V.P., 2007. Age and tectonic position of plagiogranites of the Sarakoksha massif (Altai Mountains). *Litosfera*, No. 6, 137–146.
- Kushiro, I., 1984. Genesis of arc magmas: a case in Japanese arcs, in: Proc. 27th International Geological Congress, Vol. 9: Petrology (Igneous And Metamorphic Rocks), pp. 259–281.
- Le Maitre, R.W., Bateman, P., Dudek, A., 1989. *A Classification of Igneous Rocks and Glossary of Terms*. Blackwell, Oxford.
- Lindsley, D.H., 1983. Pyroxene thermometry. *Am. Mineral.* 68, 477–493.
- Lytwyn, J., Casey, J., Gilbert, S., 1997. Arc-like mid-oceanic ridge basalt formed seaward of a trench-forearc system just prior to ridge subduction: An example from subaccreted ophiolites in southern Alaska. *J. Geophys. Res.* 102 (B5), 10,225–10,243.
- Lytwyn, J., Lockhart, S., Casey, J., Kusky, T., 2000. Geochemistry of near-trench intrusive associated with ridge subduction, Seldovia Quadrangle, southern Alaska. *J. Geophys. Res.* 105 (B12), 27,957–27,978.
- Maruyama, S., Santosh, M., Zhao, D., 2007. Superplume, supercontinent and post-perovskite: Mantle dynamics and anti-plate tectonics on the Core-Mantle boundary. *Gondw. Res.* 11, 7–37.
- McCulloch, M.T., Gamble, A.J., 1991. Geochemical and geodynamical constraints on subduction zone magmatism. *Earth Planet. Sci. Lett.* 102, 358–374.
- Mercier, J.-C.C., 1981. Single-pyroxene thermobarometry. *Tectonophysics* 70, 1–37.
- Miyashiro, A., 1973. The Troodos ophiolitic complex was probably formed in an island arc. *Earth Planet. Sci. Lett.* 19, 218–224.
- Nalivkin, D.V., 1983. Geological Map of the USSR and Adjacent Water Areas. Scale 1/2,500,000 [in Russian]. USSR Ministry of Geology.
- Nimis, P., Taylor, W., 2000. Single clinopyroxene thermobarometry for garnet peridotites. Part 1. Calibration and testing of a Cr-in-Cpx barometer and an enstatite-in-Cpx thermometer. *Contrib. Mineral. Petrol.* 139, 541–554.
- Nisbet, E.G., Pearce, J.A., 1977. Clinopyroxene composition in mafic lavas from different tectonic setting. *Contrib. Mineral. Petrol.* 63, 149–160.
- Phedorin, M.A., Bobrov, V.A., Chebykin, E.P., Goldberg, E.L., Melgunov, M.S., Filipova, S.V., Zolotarev, K.V., 2000. Comparison of synchrotron radiation X-ray fluorescence with conventional techniques for the analysis of sedimentary samples. *Geostandarts Newsletter* 24 (2), 205–216.
- Pin, C., Zalduendi, J.F.S., 1997. Sequential separation of light rare-earth elements, thorium and uranium by miniaturized extraction chromatography: Application to isotopic analyses of silicate rocks. *Anal. Chim. Acta* 339, 79–89.

- Pin, C., Briot, D., Bassin, C., Poitrasson, F., 1994. Concomitant separation of strontium and samarium-neodymium for isotopic analysis in silicate samples, based on specific extraction chromatography. *Anal. Chim. Acta* 298, 209–217.
- Polat, A., Kerrich, R., Wyman, D.A., 1998. The Late Archean Schreiber–Helmo and White River–Dayohessarah greenstone belts, Superior Province: collages of oceanic plateaus, oceanic arcs and subduction-accretion complexes. *Tectonophysics* 289, 295–326.
- Polat, A., Kerrich, R., Wyman, D., 1999. Geochemical diversity in oceanic komatiites and basalts from the late Archean Wawa greenstone belts, Superior Province, Canada: trace element and Nd isotope evidence for a heterogeneous mantle. *Precamb. Res.* 94, 139–173.
- Postnikov, A.A., Terleev, A.A., 2004. Neoproterozoic stratigraphy of the Altai–Sayan Folded Area. *Geologiya i Geofizika (Russian Geology and Geophysics)* 45 (3), 295–310 (269–283).
- Regelous, M., Hofmann, A.W., Abouchami, W., Galer, S.J.G., 2003. Geochemistry of lavas from the Emperor seamounts, and the geochemical evolution of Hawaiian magmatism from 85 to 42 Ma. *J. Petrology* 44 (1), 113–140.
- Repina, L.N., Romanenko, E.V., 1978. Trilobites and Lower Cambrian Stratigraphy of Altai [in Russian]. Nauka, Moscow.
- Safonova, I.Yu., 2008. Geochemical evolution of the Paleo-Asian Ocean intra-plate magmatism from the Late Neoproterozoic to the Early Cambrian. *Petrology* 16, 492–511.
- Safonova, I.Yu., 2009. Intraplate magmatism and oceanic plate stratigraphy of the Paleo-Asian and Paleo-Pacific Oceans from 600 to 140 Ma. *Ore Geol. Rev.* 35, 137–154.
- Safonova, I.Yu., Buslov, M.M., Iwata, K., Kokh, D.A., 2004. Fragments of Vendian-Early Carboniferous oceanic crust of the Paleo-Asian Ocean in foldbelts of the Altai–Sayan region of Central Asia: geochemistry, biostratigraphy and structural setting. *Gondw. Res.* 7 (3), 771–790.
- Safonova, I.Yu., Simonov, V.A., Buslov, M.M., Ota, T., Maruyama, Sh., 2008. Neoproterozoic basalts of the Paleo-Asian Ocean (Kurai accretionary zone, Gorny Altai, Russia): geochemistry, petrogenesis, and geodynamics. *Russian Geology and Geophysics (Geologiya i Geofizika)* 49 (4), 254–271 (335–356).
- Safonova, I.Yu., Utsunomiya, A., Kojima, S., Nakae, S., Tomurtogoo, O., Filippov, A.N., Koizumi, K., 2009. Pacific superplume-related oceanic basalts hosted by accretionary complexes of Central Asia, Russian Far East and Japan. *Gondw. Res.* 16, 587–608.
- Saunders, A.D., Norry, M.J., Tarney, J., 1988. Origin of MORB and chemically-depleted mantle reservoirs: trace element constrains. *J. Petrology, Spec. Lithosphere Issue*, 415–455.
- Sheth, H.C., Melluso, L., 2008. The Mount Pavagadh volcanic suite, Deccan Traps: Geochemical stratigraphy and magmatic evolution. *J. Asian Earth Sci.* 32 (15), 5–21.
- Shokalsky, S.P., Babin, G.A., Vladimirov, A.G., Borisov, S.M., 2000. Correlation of Magmatic and Metamorphic Complexes in Western Altai–Sayan [in Russian]. Izd. SO RAN, Filial “Geo”, Novosibirsk.
- Simonov, V.A., Al’ mukhamedov, A.I., Kovyazin, S.V., Medvedev, A.Ya., Tikunov, Yu.V., 2004. Conditions of petrogenesis of boninites in ophiolites of the Dzhida zone, northern Mongolia (*from data on melt inclusions*). *Geologiya i Geofizika (Russian Geology and Geophysics)* 45 (6), 651–662 (605–617).
- Simonov, V.A., Kovyazin, S.V., Vasil’ev, Yu.R., Mahoney, J., 2005. Physicochemical parameters of continental and oceanic plateau-basalt magmatic systems (from data on melt inclusions). *Russian Geology and Geophysics (Geologiya i Geofizika)* 46 (9), 886–903 (908–923).
- Sobolev, A.V., 1996. Melt inclusions in minerals as a source of principal petrological information [in Russian]. *Petrologiya* 4 (3), 209–220.
- Sobolev, A.V., Sobolev, S.V., Kuzmin, D.V., Malitch, K.N., Petrunin, A.A., 2009. Siberian meimechites: origin and relation to flood basalts and kimberlites. *Russian Geology and Geophysics (Geologiya i Geofizika)* 50 (12), 999–1033 (1293–1335).
- Sun, S., McDonough, W.F., 1989. Chemical and isotopic systematics of oceanic basalts: Implications for mantle composition and processes, in: Saunders, A.D., Norry M.J. (Eds.), *Magmatism in the Ocean Basins*. Geological Society London, Spec. Publ. 42, pp. 313–345.
- Tatsumi, T., Shukuno, H., Yoshikawa, M., Chang, Q., Sato, K., Lee, M.W., 2005. The petrology and geochemistry of volcanic rocks on Jeju Island: Plume magmatism along the Asian continental margin. *J. Petrology* 46 (3), 523–553.
- Tatsumi, Y., 1991. Origin of subduction zone magmas based on experimental petrology, in: Perchuk, L.L., Kushiro, I. (Eds.) *Physical Chemistry of Magma*. Springer-Verlag, Vol. 9, pp. 268–301.
- Taylor, S.R., McLennan, S.M., 1985. *The Continental Crust: Its Composition and Evolution*. Blackwell Scientific Publication, Oxford.
- Thompson, G., 1991. Metamorphic and hydrothermal processes: basalt-seawater interactions, in: Floyd, P.A. (Ed.), *Oceanic Basalts*. Blachie and Sons Ltd., Glasgow, pp. 148–173.
- Thorkelson, D.J., 1994. Ridge subduction: kinematics and implications for the nature of mantle upwelling: Discussion. *Can. J. Earth Sci.* 31, 1486–1489.
- Thurson, P.C., 2002. Autochthonous development of Superior Province greenstone belts? *Precamb. Res.* 115, 11–36.
- Utsunomiya, A., Jahn, B.-m., Ota, T., Safonova, I.Yu., 2009. A geochemical and Sr–Nd isotopic study of the Vendian greenstones from Gorny Altai, southern Siberia: Implications for the tectonic setting of the formation of greenstones and the role of oceanic plateaus in accretionary orogen. *Lithos* 113, 437–453.
- Vrublevskii, V.V., Izokh, A.E., Polyakov, G.V., Gertner, I.F., Yudin, D.S., Krupchatnikov, V.I., 2009. Early Paleozoic alkaline magmatism of the Altai Mountains: ⁴⁰Ar–³⁹Ar geochronology data for the Edel’veis complex. *Dokl. Earth Sci.* 427 (5), 846–850.
- Weaver, S.D., Johnson, R.W. (Eds.), 1987. *Tectonic Controls on Magma Chemistry*. Elsevier, Amsterdam.
- Weaver, B.L., 1991. The origin of ocean island basalts and member compositions: trace element and isotopic constrains. *Earth Planet. Sci. Lett.* 104, 381–397.
- Winchester, J.A., Floyd, P.A., 1977. Geochemical discrimination of different magma series and their differentiation products using immobile elements. *Chem. Geol.* 20, 325–343.
- Yokoyama, T., Makishima, A., Nakamura, E., 1999. Evaluation of the coprecipitation of incompatible trace elements with fluoride during silicate rock dissolution by acid digestion. *Chem. Geol.* 157, 175–187.
- Zindler, A., Hart, S.R., 1986. Chemical geodynamics. *Ann. Rev. Earth Planet. Sci.* 14, 493–571.
- Zolotukhin, V.V., Al’ mukhamedov, A.I., 1988. Traps of the Siberian platform, in: McDougall, J.D. (Ed.), *Continental Flood Basalts*. Kluwer Academic Publishers, Dordrecht, pp. 273–310.
- Zybin, V.A., 2006. Etalon of the Ust’-Sema Complex of Porphyric Basalts and Trachybasalts (Gorny Altai) [in Russian]. SNIIGiMS, Novosibirsk.